A New Pathway for Tornadogenesis Exposed by Numerical Simulations of Supercells in Turbulent Environments

PAUL M. MARKOWSKI[a]

[a] *Department of Meteorology and Atmospheric Science, The Pennsylvania State University, University Park, Pennsylvania*

(Manuscript received 14 September 2023, in final form 6 December 2023, accepted 3 January 2024)

ABSTRACT: A simulation of a supercell storm produced for a prior study on tornado predictability is reanalyzed for the purpose of examining the fine-scale details of tornadogenesis. It is found that the formation of a tornado-like vortex in the simulation differs from how such vortices have been understood to form in previous numerical simulations. The main difference between the present simulation and past ones is the inclusion of a turbulent boundary layer in the storm's environment in the present case, whereas prior simulations have used a laminar boundary layer. The turbulent environment contains significant near-surface vertical vorticity ($\zeta > 0.03\ s^{-1}$ at $z = 7.5$ m), organized in the form of longitudinal streaks aligned with the southerly ground-relative winds. The ζ streaks are associated with corrugations in the vertical plane in the predominantly horizontal, westward-pointing environmental vortex lines; the vortex-line corrugations are produced by the vertical drafts associated with coherent turbulent structures aligned with the aforementioned southerly ground-relative winds (longitudinal coherent structures in the surface layer such as these are well known to the boundary layer and turbulence communities). The ζ streaks serve as focal points for tornadogenesis, and may actually facilitate tornadogenesis, given how near-surface ζ in the environment can rapidly amplify when subjected to the strong, persistent convergence beneath a supercell updraft.

SIGNIFICANCE STATEMENT: In high-resolution computer simulations of supercell storms that include a more realistic, turbulent environment, the means by which tornado-like vortices form differs from the mechanism identified in prior simulations using a less realistic, laminar environment. One possibility is that prior simulations develop intense vortices for the wrong reasons. Another possibility could be that tornadoes form in a wide range of ways in the real atmosphere, even within supercell storms that appear to be similar, and increasingly realistic computer simulations are finally now capturing that diversity.

KEYWORDS: Convective storms/systems; Tornadogenesis; Turbulence; Large eddy simulations

1. Introduction

a. *A brief summary of our current understanding of tornadogenesis in supercell storms*

Tornado formation in supercell thunderstorms is among the most intensely studied problems in mesoscale meteorology,[1] as evidenced by the numerous reviews that have been written on the subject (Ludlam 1963; Rotunno 1993; Davies-Jones and Brooks 1993; Davies-Jones et al. 2001; Markowski and Richardson 2009, 2014a; Davies-Jones 2015). More studies have been devoted to supercell tornadoes than nonsupercell tornadoes, presumably because the former are associated with the most destructive tornadoes.

Our latest understanding of supercell tornadogenesis can be summarized as follows. The supercell initially acquires updraft-scale rotation (about a vertical axis) via the updraft's upward bending of horizontal vortex lines present in the vertically sheared environment. Mature supercell storms, owing to the dynamic vertical perturbation pressure gradient force (VPPGF) field, tend to propagate to the right of the mean environmental wind (Rotunno and Klemp 1982, 1985), and as a result, the storm-relative inflow into a mature supercell storm tends to have a significant component aligned with the aforementioned environmental horizontal vorticity. The presence of a storm-relative streamwise vorticity component leads to the supercell's updraft having net cyclonic rotation (Davies-Jones 1984), as opposed to a vertical vorticity (ζ) couplet straddling the updraft (and thus no net rotation) when crosswise horizontal vorticity is tilted.

Davies-Jones (1982a,b) hypothesized that the upward tilting of environmental vortex lines that leads to the so-called midlevel mesocyclone[2] cannot yield a tornado because the upward tilting of the horizontal vorticity is occurring only as air

[1] Strictly speaking, tornadoes are microscale phenomena (Orlanski 1975; Fujita 1981), but their parent thunderstorms are usually regarded as mesoscale phenomena.

Supplemental information related to this paper is available at the Journals Online website: https://doi.org/10.1175/JAS-D-23-0161.s1.

Corresponding author: Paul Markowski, pmarkowski@psu.edu

[2] "Mesocyclone aloft" might be a better term, given that in exceptionally strong environmental vertical shear, the tilting of environmental vortex lines can yield mesocyclone-strength ζ ($\gtrsim 0.01\ s^{-1}$) at cloud base (e.g., Coffer et al. 2023).

DOI: 10.1175/JAS-D-23-0161.1

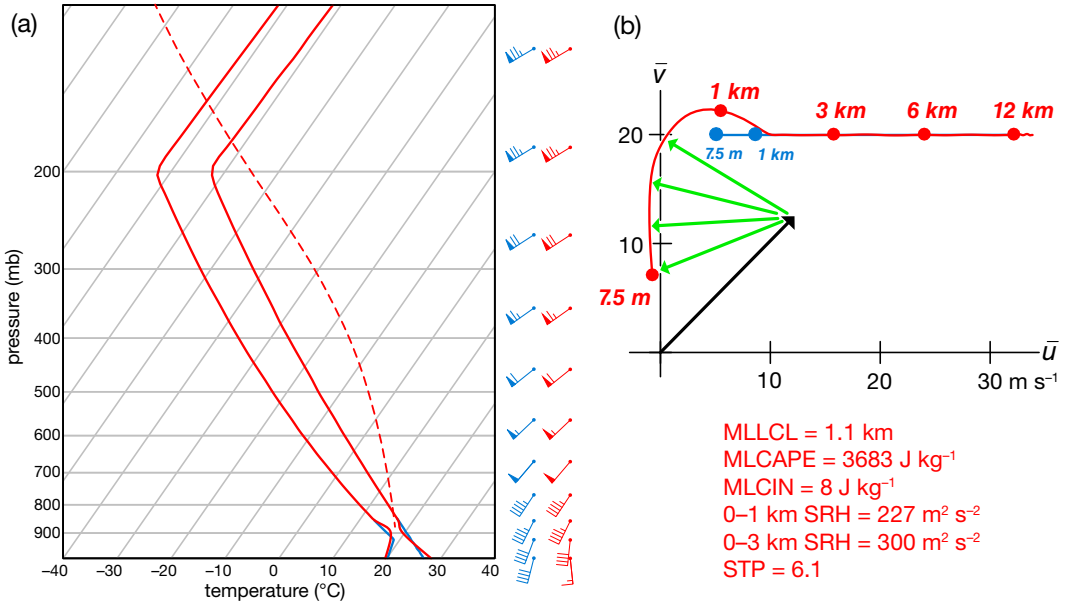

FIG. 1. (a) Domain-averaged soundings and ground-relative vertical wind profiles in the initial environment (blue) and quasi-steady environment after the 12-h spinup period, i.e., at the time that a warm bubble is introduced in order to initiate convection (red). Wind barbs are in knots. The dashed red curve is the pseudoadiabat followed by a parcel having the mean thermodynamic properties of the lowest 1 km. (b) Hodographs depicting the domain-averaged vertical wind profiles at $t = 0$ h (blue) and $t = 12$ h (red). Units on the axes are m s^{-1}; select altitudes along the hodographs are labeled ($z = 7.5$ m, 1, 3, 6, and 12 km). The black arrow indicates the ensemble mean storm motion. The green arrows indicate the storm-relative winds in the lowest 500 m. In both (a) and (b), the mean environments are independent of the random number seed used to impose random temperature perturbations at $t = 0$ h (i.e., the soundings and hodographs depict the mean environments in every ensemble member). The environmental parameters displayed in the lower right portion of the figure are for the quasi-steady environment at $t = 12$ h. MLLCL, MLCAPE, and MLCIN refer to mixed-layer (ML) lifting condensation level (LCL), CAPE, and convective inhibition (CIN), respectively. These were computed by lifting a parcel having the mean thermodynamic properties of the lowest 1 km. Adapted from M20.

rises away from the surface. Of course, once a tornado is established, inflow into the base of the vortex—and the vortex lines embedded in that inflow—turn upward at a ~90° angle to yield large ζ next to the surface. But Davies-Jones argued that such extreme tilting of vortex lines cannot occur until a tornado is established, and thus, the tilting of environmental vortex lines by the supercell updraft alone cannot be relied upon as a tornado *genesis* mechanism. For this reason, Davies-Jones hypothesized that the development of large ζ next to the surface, in environments lacking initial near-surface ζ (the convergence of planetary vorticity also has been assumed not to be a significant ζ source for the tornado; e.g., Davies-Jones 2015) ought to involve air parcels that have descended through downdrafts. Within downdrafts, vorticity can be tilted upward even as air descends (e.g., Davies-Jones and Brooks 1993), thereby circumventing the limitation of parcels only acquiring ζ in an updraft once they have risen away from the surface.

Numerical simulations of supercell storms, and observations where available, have supported the notion that downdrafts are critical for the development of near-surface ζ, including tornadoes, in supercells (Markowski 2002). Moreover, simulations have revealed that horizontal buoyancy gradients associated with the downdrafts are a key vorticity source (e.g., Klemp and Rotunno 1983; Rotunno and Klemp 1985; Davies-Jones and Brooks 1993; Adlerman et al. 1999; Markowski and Richardson 2014b; Dahl et al. 2014; Parker and Dahl 2015). The horizontal buoyancy gradients, which generate horizontal vorticity baroclinically, owe their existence to the density variation between the warm environment and the negative buoyancy in the precipitation region; the latter is due to latent cooling (mostly evaporation, though melting and sublimation also contribute) and hydrometeor mass. Depending on the orientation of the baroclinic zones and air parcel residence times, the baroclinically generated horizontal vorticity can be quite significant relative to (and potentially augment) the environmental horizontal vorticity.

The horizontal vorticity within the rain-cooled air parcels can develop a vertical component via tilting, either while parcels are descending (Davies-Jones and Brooks 1993; Adlerman et al. 1999; Dahl et al. 2014; Parker and Dahl 2015), or once parcels begin rising owing to the influence of the dynamic VPPGF associated with the overlying rotating updraft (Rotunno et al. 2017; Boyer and Dahl 2020; Fischer and Dahl 2022). Tornado-like

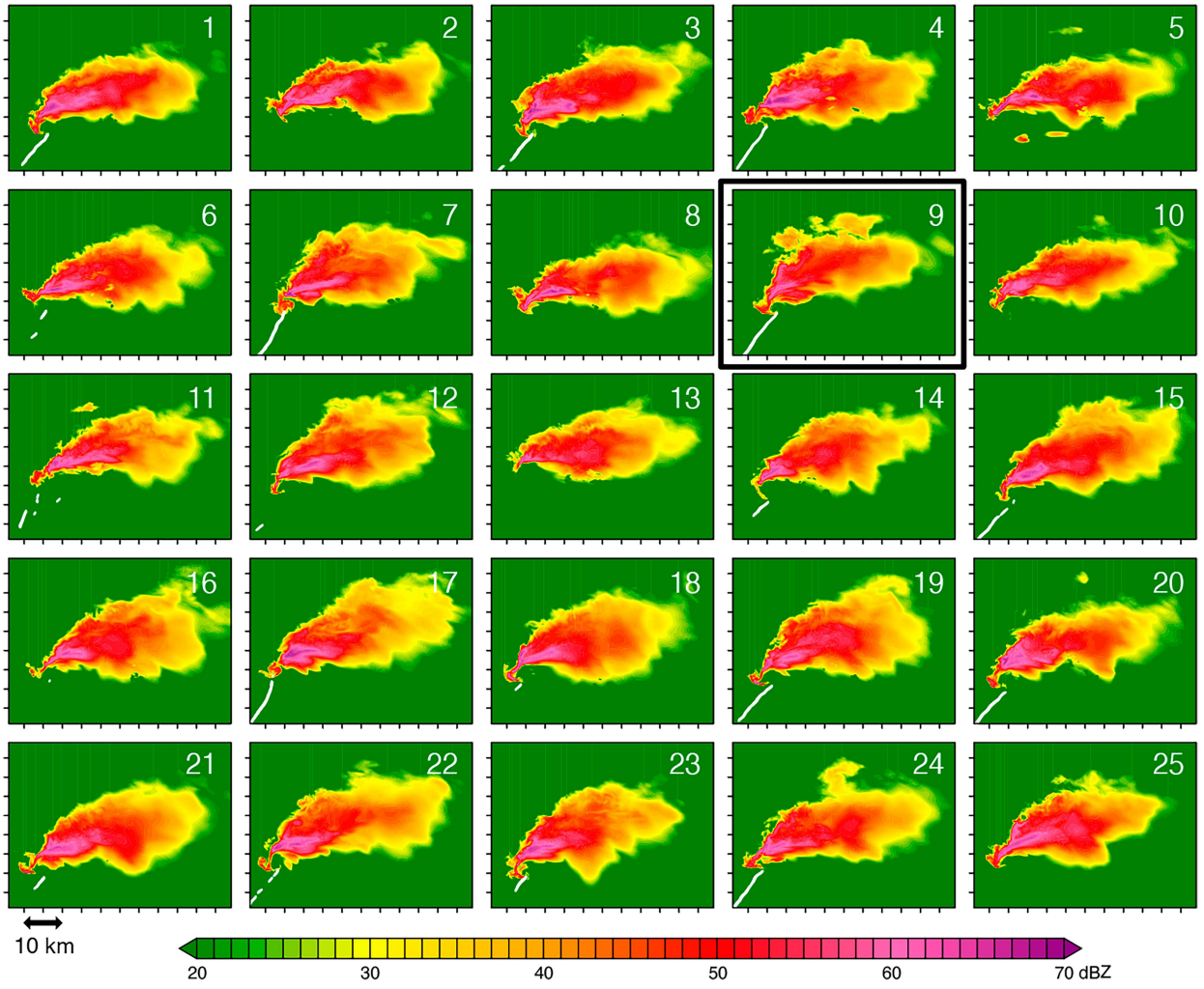

FIG. 2. Reflectivity at $z = 993$ m at 7200 s in each of the M20 ensemble members. White swaths are tornado tracks (the storms are approximately stationary on the model grid; the tracks are plotted by converting tornado locations to ground-relative locations). The numerals in each panel indicate the identification number of the ensemble member. Ensemble member number 9, the focus of this article, is indicated by the bold box. Adapted from M20.

vortices (TLVs)[3] can develop in numerically simulated storms if the near-surface ζ is subsequently increased via stretching (e.g., Markowski and Richardson 2014b; Guarriello et al. 2018; Boyer and Dahl 2020). Tornadogenesis in supercells has been viewed as a "Goldilocks" problem: downdrafts and outflow are seen as being critical for the initial development of near-surface ζ, but not in excess, lest the upward accelerations that are subsequently necessary for the explosive growth of ζ are inhibited by excessive negative buoyancy (Markowski and Richardson 2014b).

[3] The term TLV is probably more appropriate than tornado when horizontal (vertical) grid spacings larger than ~25 m (~10 m) are used, given what is required to resolve aspects of the wind field that are unique to tornadoes (e.g., corner flow region, near-surface vertical jets, suction vortices; Lewellen 1993).

b. *A critique of our current understanding of tornadogenesis in supercell storms*

Though the summary above seems rather compelling and has been the basis for many review articles in recent decades, vorticity and circulation budgets in observed storms have proven difficult to obtain owing to the challenges in obtaining buoyancy observations, especially above the ground, in addition to the errors in dual-Doppler wind syntheses (dual-Doppler retrieval errors are exacerbated in vorticity budget calculations owing to the presence of products of velocity derivatives). There are also plenty of reasons to be skeptical of past numerical simulations. Many of the simulations in the late twentieth century used microphysics schemes that might have enhanced the baroclinic zones (Markowski 2002). Moreover, until roughly the last decade, the vast majority of supercell simulations employed a free-slip lower boundary

condition (Klemp and Wilhelmson 1978; Wilhelmson and Wicker 2001). In relatively recent supercell simulations by Schenkman et al. (2014), Roberts et al. (2016, 2020), Roberts and Xue (2017), Yokota et al. (2018), and Tao and Tamura (2020), which have employed more sophisticated microphysics schemes and a semislip (i.e., bulk drag) lower boundary condition, horizontal vorticity generation by surface friction, with subsequent tilting and stretching, has been implicated in the formation of TLVs, though downdrafts were likely still critical for TLV formation in at least some, if not all of these simulations (e.g., Schenkman et al. 2014).

Although numerical simulations have been vital to our growth in understanding of supercells and tornadogenesis over the last half century, it is fair to say that all supercell simulation results have sensitivities, ranging from mild to severe, to the physical parameterizations, most notably the microphysics and lower boundary condition. With respect to the latter, it is more than just an issue of free-slip versus semislip. The assumptions involved in the formulation of the semislip lower boundary condition are themselves questionable, as discussed by Markowski (2016), Markowski and Bryan (2016), Markowski et al. (2019), and Wang et al. (2020, 2023).

Another potentially serious omission in past simulations stands out: lack of turbulence in the storm environment. Prior studies have simulated storms almost exclusively in laminar environments, either because the horizontal resolution was marginal or inadequate (e.g., grid spacings $\gtrsim$100 m), or, even when it was adequate, a mechanism for triggering turbulence was absent (e.g., Orf et al. 2017). Of course, in prior simulations, turbulence is present *within* the storm and its outflow, though the magnitudes of resolved versus subgrid-scale (SGS) turbulence can be problematic, depending on the resolution (that is an entirely different issue). This article is about the effects of *resolved, coherent turbulent structures in the storm environment*, particularly the surface layer, on TLV formation, and by extension, tornadogenesis.

c. *The M20 simulations*

Markowski (2020, hereafter M20) created a 25-member ensemble of relatively high-resolution (Δx = 75 m, minimum Δz = 15 m; Δx and Δz are the horizontal and vertical grid spacings) numerical simulations of tornadic supercell storms using Cloud Model version 1 (CM1; Bryan and Fritsch 2002) in order to study their intrinsic predictability. Small random temperature perturbations present in the initial conditions triggered turbulence within the boundary layers. The turbulent boundary layers were given 12 h to evolve to a quasi-steady state before storms were initiated via the introduction of a warm bubble. There was no surface heat flux; thus, the quasi-steady boundary layer might best be regarded as a late-day boundary layer near the time of the early evening transition, which is when tornadoes are most likely anyway, at least in the U.S. Great Plains region (Anderson-Frey et al. 2017). The spatially averaged environments—which were extremely favorable for tornadoes [e.g., large and directionally varying wind shear, substantial convective available potential energy (CAPE), high boundary layer relative humidity]—were identical within the ensemble (Fig. 1). Only the random number seed and/or warm bubble location were varied.

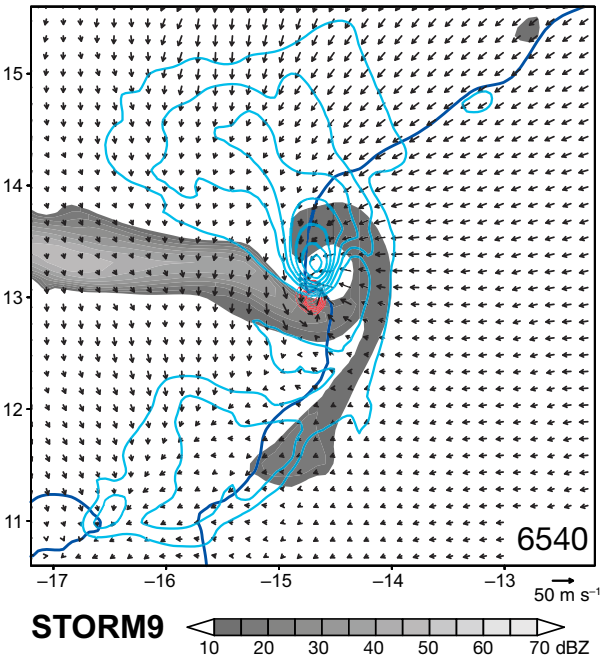

FIG. 3. The tornadic region in M20's ensemble member number 9 at 6540 s, at which time the TLV is at its peak intensity. Reflectivity (gray shading) and vertical velocity (cyan contours of 6, 12, 18 m s^{-1}, etc.) are displayed at z = 993 m. Horizontal storm-relative velocity vectors (every second grid point) and vertical vorticity (red contours of 0.1, 0.2, 0.3 s^{-1}, etc.) are displayed at z = 7.5 m. The $\theta'_\rho = -0.25$ K isopleth (dark blue contour) is overlaid to serve as a proxy for the gust-front location. Axis labels are in kilometers.

All of the simulated storms were long-lived supercells with intense updrafts and strong mesocyclones extending to the lowest model level (z = 7.5 m). Even the storms with the weakest near-surface rotation probably could be regarded as weakly tornadic. However, despite the statistically identical environments, there was considerable divergence in the fine-scale details of the simulated storms (Fig. 2). The intensities of the TLVs that developed in the simulations ranged from EF0 to EF3, with large differences in formation time and duration also being exhibited. All of the simulation differences were ultimately attributable to differences in how the initial warm bubbles and/or storms interacted with turbulent boundary layer structures. The results suggested very limited intrinsic predictability with respect to predicting the formation time, duration, and intensity of tornadoes.

The M20 study focused on the predictability rather than the dynamics of tornadogenesis. The tornadic supercells in the M20 simulations all looked rather ordinary relative to the existing body of literature (Fig. 3), possessing classic features such as a hook echo, cool air wrapping around the tornado, an occluded gust-front structure, and a kidney-bean-shaped low-level updraft overlying the tornado (Lemon and Doswell 1979; Doswell and Burgess 1993). There was no

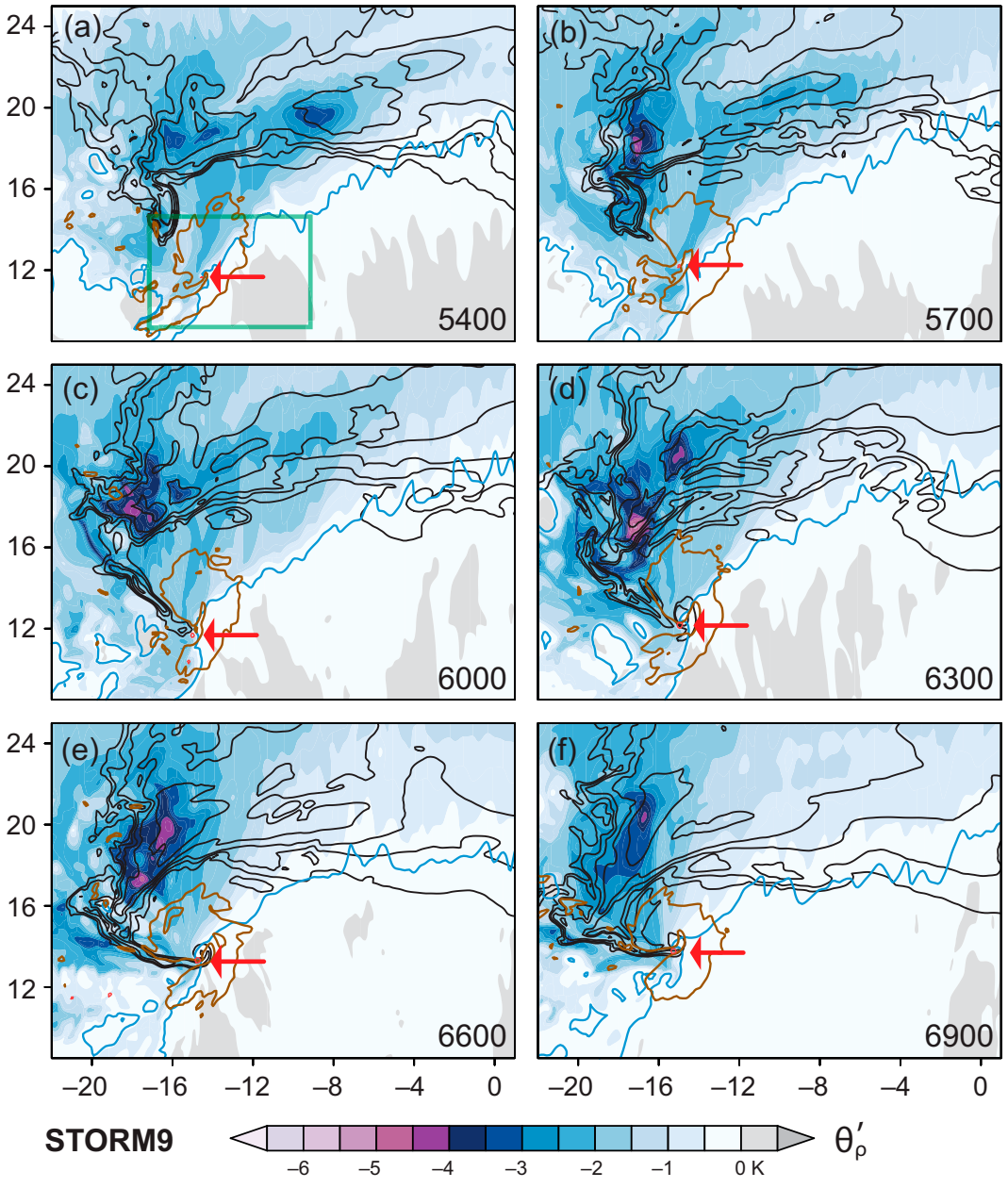

FIG. 4. Horizontal cross sections of θ_ρ' at z =7.5 m (shaded), the w = 6 m s^{-1} isotach at z = 993 m (brown contours), the ζ = 0.10 s^{-1} isovort at z = 7.5 m (red contours, red arrows point to it), and reflectivity at z = 522 m (black contours of 20, 30, 40, 50, and 60 dBZ) from (a) 5400 to (f) 6900 s at 300-s intervals in the STORM9 simulation. The θ_ρ' = −0.25 K isopleth (bold blue contours) is overlaid to serve as a proxy for the gust front location. Axis labels are in kilometers. The box overlaid in (a) encloses the zoomed-in region shown in Fig. 5.

reason to think that the dynamics of tornado formation in the M20 simulations differed from the longstanding conceptual model summarized in section 1a, microphysics and lower-boundary condition uncertainties aside (these are unavoidable in all simulations). A closer inspection of the M20 simulations reveals a different story, however.

In this article, it will be shown that tornado formation in at least one of the M20 simulations ("storm 9") proceeds differently than how supercell tornado formation has been envisioned to date, and that resolved, coherent, turbulent structures in the surface layer of the storm's environment are key. Such features have not been present in prior simulations, and are unfortunately not resolved in prior observational studies, or may not even be observed, depending on a radar's clear-air sensitivity. Nowotarski et al. (2015) is the only other supercell simulation in which a turbulent

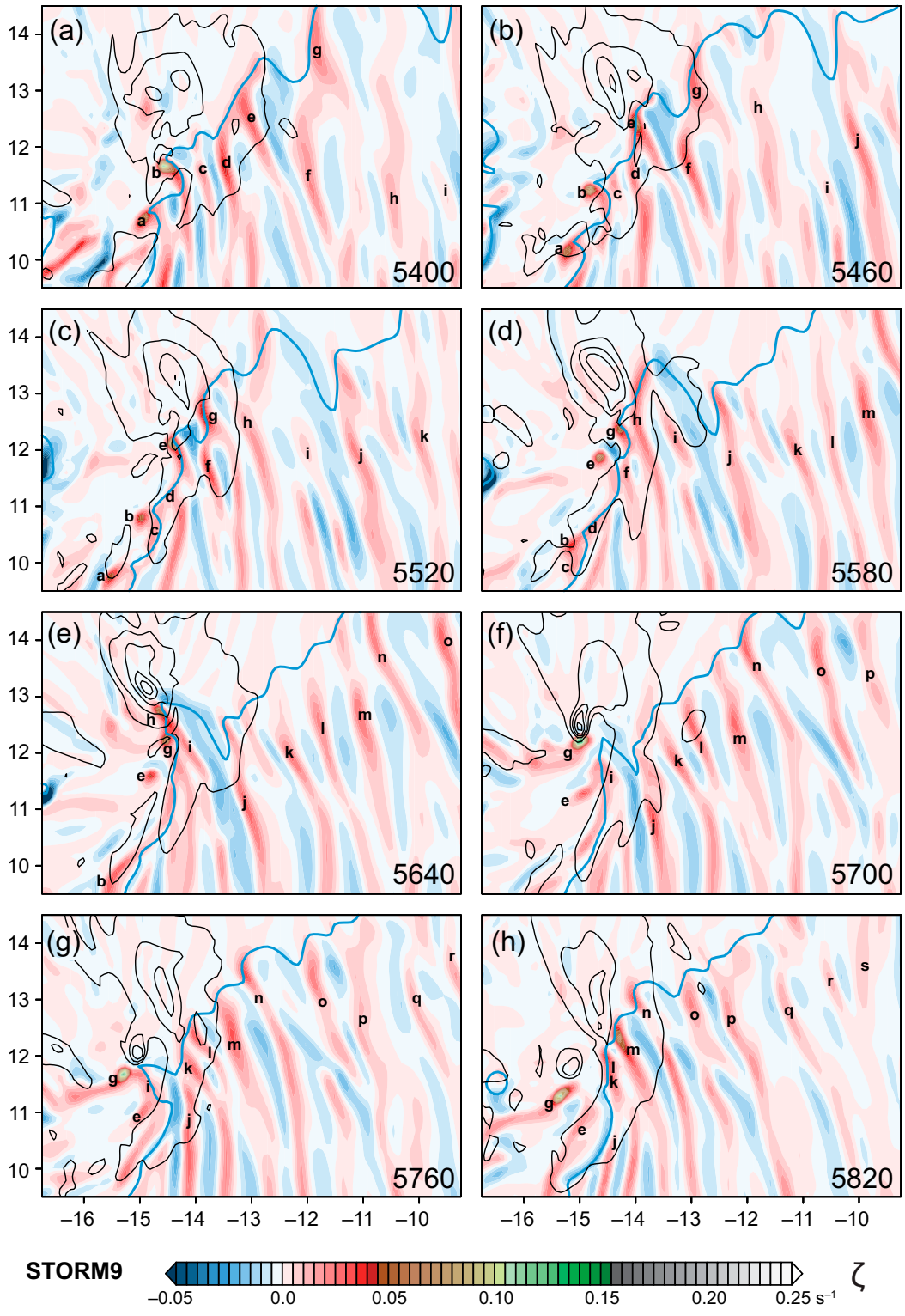

FIG. 5. Horizontal cross sections of ζ at z =7.5 m (shaded) and w at z = 522 m (black isotachs of 5, 10, 15, 20, 25 m s^{-1}) from (a) 5400 to (p) 6300 s at 60-s intervals in the STORM9 simulation. The $\theta'_\rho = -0.25$ K isopleth (bold blue contours) is overlaid to serve as a proxy for the gust front location. Axis labels are in kilometers. Letters identify particular ζ maxima to facilitate their tracking from panel to panel; the "m" anomaly attains TLV ζ and wind speed thresholds at 6240 s.

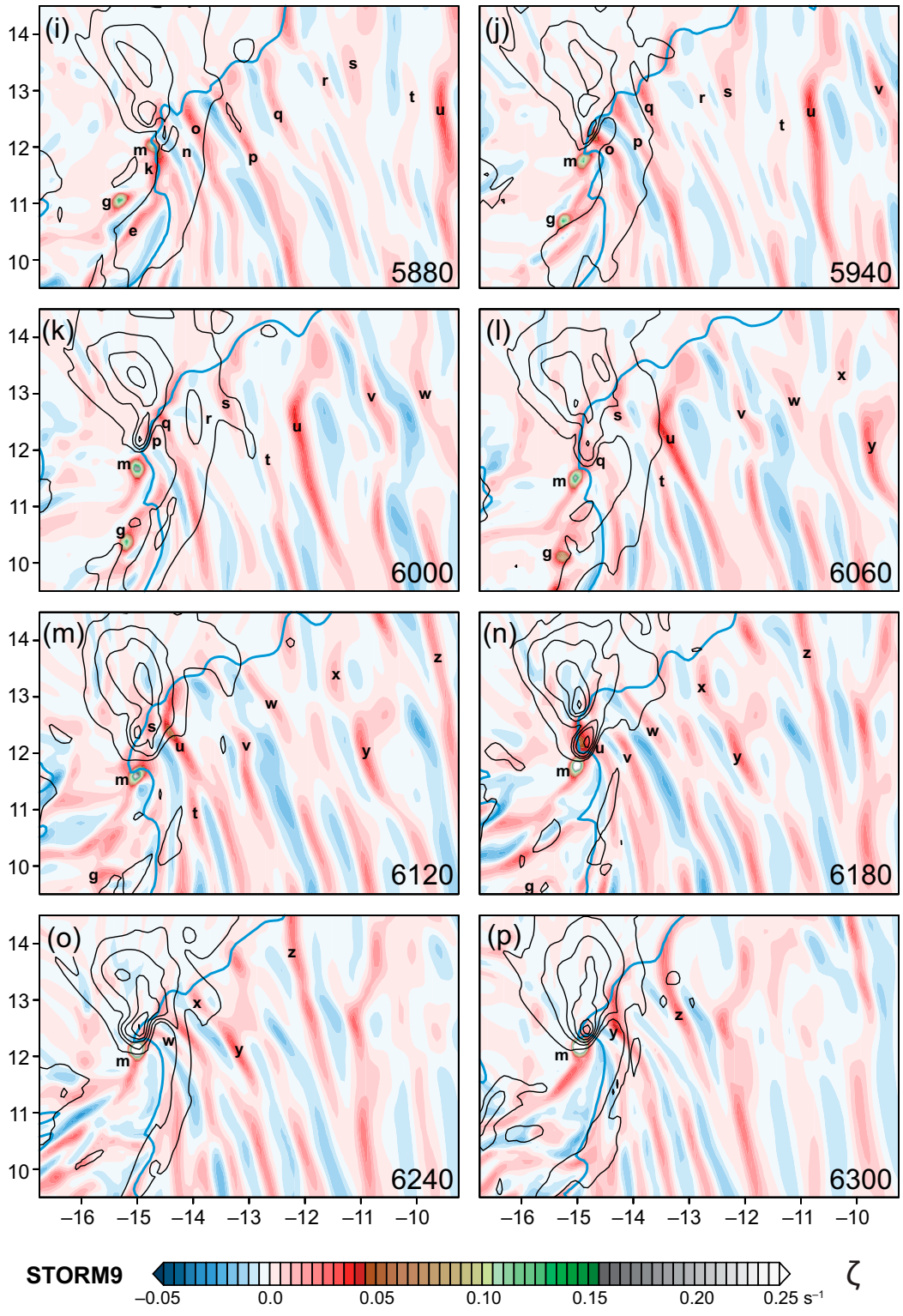

FIG. 5. (*Continued*)

environmental boundary layer was present, but the resolution was somewhat coarser (Δx = 200 m, Δz = 50 m) than that of the M20 simulations.

The analysis of tornadogenesis in this storm is presented in section 2, and a pair of ancillary simulations are presented in section 3. The implications are discussed in section 4. Concluding remarks are provided in section 5. A pair of appendices contain, respectively, a summary of the numerical model configuration (appendix A), which is the same as used by M20, and an explanation of the presence of an "invented" force (Davies-Jones 2021) in the M20 simulations (appendix B).

2. TLV genesis in the STORM9 simulation

a. Overview of ensemble member number 9

All of the storms in the M20 ensemble are long-lived supercells that produce at least brief TLVs. Ensemble members number 3 and 9 (M20's Fig. 9) contain the most intense TLVs (61.6 m s^{-1} peak 10-m wind). However, the timing of TLV formation varies considerably within the ensemble, and TLV intensity ranges from EF0 to EF3, despite all of the simulated storms being in statistically identical environments, thereby suggesting rather limited intrinsic predictability with respect to predicting the formation time, duration, and intensity of tornadoes. As explained in M20, the simulation differences only can be explained by differences in how the initial warm bubbles and/or storms interact with turbulent boundary layer structures.

The present study investigates the fine-scale aspects of TLV formation in a rerun of M20's ensemble member number 9 (Figs. 2 and 3). The rerun simulation, hereafter referred to as the STORM9 simulation, was performed in order to produce output at 30-s intervals, as the original M20 study only produced 300-s output. The 300-s output was sufficient for the goals of M20, but not for the present study (again, the focus of M20 was predictability and the distribution of TLV characteristics within the ensemble, not the exact reproducibility of any particular realization). Though M20's use of an adaptive time step would ordinarily lead to reproducibility issues when changing the output frequency (the time step considers the Courant number, but also is adjusted so that time steps land on user-specified output times), reducing the output frequency to 30 s had no appreciable effect on the time steps and simulation.[4] This is because extrema statistics (e.g., maximum ζ) were saved every 30 s in the original M20 simulation, even though the gridded output was saved only every 300 s.

Similarity between the original M20 simulation and the rerun is not strictly necessary for the present study, but there is obviously a desire for the rerun simulation to at least produce an intense TLV. It is debatable whether 30-s data are sufficiently fine for some aspects of the study of TLV genesis (e.g., budget calculations along material circuits); unfortunately, an attempt to rerun the STORM9 simulation with 10-s output resulted in a storm that produced a substantially weaker (EF1) TLV. (This sensitivity to time step is yet another testament to the limited intrinsic predictability of tornadic supercells documented by M20.) Nonetheless, it will be evident that 30-s output is sufficient for the analyses performed herein, even when it comes to reconciling the circulation budgets of the material circuits analyzed in section 2e.

b. Evolution of the vertical vorticity field

The evolution of the STORM9 simulation's storm-scale reflectivity, density potential temperature perturbation (θ'_ρ; Emanuel 1994, p. 161), and low-level updraft fields from 5400 to 6900 s is presented in Fig. 4. All times refer to the time elapsed since the introduction of the storm-initiating warm bubble after the 12-h spinup simulation. The structure and evolution of the simulated storm (e.g., Figs. 3 and 4) are no different from what has been documented in observed and simulated supercells dating back to the discovery of supercell storms, with classic features such as a hook echo (Stout and Huff 1953; Fujita 1958, 1973; Browning 1965; Lemon and Doswell 1979; Forbes 1981; Klemp et al. 1981), occluded gust-front structure (Brandes 1978, 1981; Klemp and Rotunno 1983; Wicker and Wilhelmson 1995; Adlerman et al. 1999), and outflow and downdraft wrapping around the vortex (Lemon and Doswell 1979; Klemp and Rotunno 1983; Davies-Jones and Brooks 1993), which lies beneath the northern flank of a kidney-bean-shaped low-level updraft (Lemon and Doswell 1979; Doswell and Burgess 1993).

Close inspection of the evolution of the near-surface ζ field reveals a humbling level of complexity (Fig. 5; see the online supplementary material for animations). Alternating streaks (wavelength ~500–700 m) of positive and negative ζ on the warm (i.e., environmental) side of the gust front are encountered by the low-level updraft. In the positive-ζ streaks, ζ frequently reaches or exceeds 0.03 s^{-1} at z = 7.5 m (the lowest grid level for horizontal velocity) in the region 5–10 km east (i.e., upstream, in a storm-relative sense). The ζ in the negative-ζ streaks is generally of lesser magnitude at z = 7.5 m (rarely less than −0.02 s^{-1}). The differences are ultimately a consequence of the inclusion of planetary vorticity. The ζ field on the cool side of the gust front also is organized into longitudinal streaks, but the magnitude of the highest amplitude plus and minus ζ perturbations is only 10%–20% of those present in the environmental air, presumably owing to the suppression of turbulence by the weak static stability here.

As the streaks near the overlying updraft of the supercell, positive ζ further amplifies within the streaks, and does so more than the negative-ζ anomalies. Several attempts at TLV genesis occur from 5400 to 5900 s within the intensifying positive-ζ anomalies as they slide beneath the overlying storm updraft (Figs. 5a–i). After a few failures, one anomaly, labeled "m" in Fig. 5, becomes "attached" to the overlying storm updraft, deepens, and intensifies in the 5940–6300-s period (Figs. 5j–p). "Axisymmetrization" of the intensifying ζ maximum—i.e., the development of closed streamlines

[4] The rerun simulation is not quite an exact match to the original simulation owing to a change in the operating system, processors, and Fortran compiler on the supercomputer between 2019 and 2022, the years when the M20 simulations and simulations performed for this study were executed. The peak 10-m wind speed is 62.7 m s^{-1} (Table 1) in the rerun simulation, compared with 61.6 m s^{-1} in M20's original.

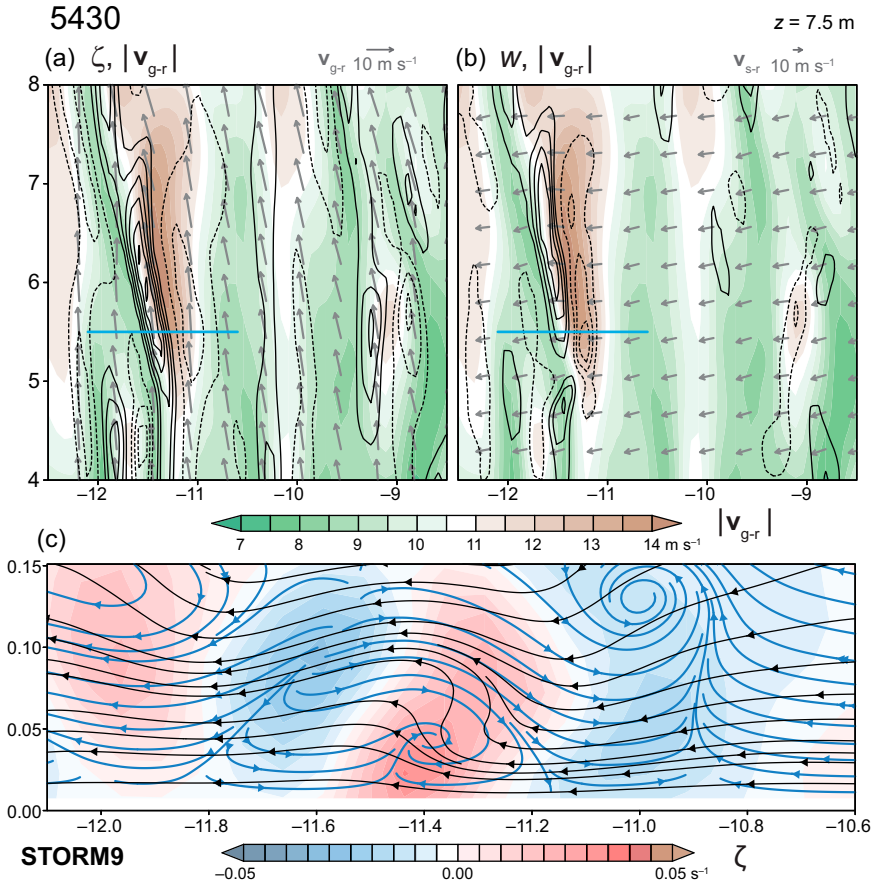

FIG. 6. (a) Horizontal cross section of ground-relative wind speed ($|\mathbf{v}_{g\text{-}r}|$; shaded) and ζ in the STORM9 simulation at $z = 7.5$ m at 5430 s in the subdomain enclosed by the square in Fig. 7; ζ is contoured every 0.005 s^{-1}, dashed contours indicate negative ζ, and the $\zeta = 0$ s^{-1} isovort is suppressed. Ground-relative horizontal velocity vectors ($\mathbf{v}_{g\text{-}r}$) also are overlaid. Axis labels are x and y positions in kilometers. (b) As in (a), but w and storm-relative horizontal velocity vectors ($\mathbf{v}_{s\text{-}r}$) are overlaid; w is contoured every 0.025 m s^{-1}, dashed contours indicate negative w, and the $w = 0$ m s^{-1} isotach is suppressed. The cyan lines overlaid in (a) and (b) indicate the location the vertical cross section shown in (c). (c) Vertical cross section of ζ (shaded), u'-w streamlines [blue arrows; u' is the zonal wind perturbation relative to the mean $u(z)$ over the horizontal span of the vertical cross section], and pseudovortex lines (black arrows; field lines of the x and z vorticity components in the plane of the cross section). Axis labels are in kilometers.

in the storm-relative reference frame, a dynamic pressure deficit, and dominance of ζ over deformation (Fischer and Dahl 2022)—occurs by 6000 s. The vortex attains TLV status[5] at 6250 s, and reaches its peak intensity (10-m wind speed maximum of 62.7 m s^{-1}) at 6540 s. The rerun simulation was extended to 3 h (the original M20 simulations were only run for 2 h), but the TLV dissipates early in the third hour (7230 s). Brief "spinups" (not analyzed) occur in the remainder of the simulation.

The takeaway is this: *positive-ζ streaks in the surface layer serve as nodes for TLV formation*. That TLV genesis can be linked to ζ perturbations in the environment (some might view this as "ζ noise") is consistent with the findings of Parker (2023), though there are limits to the comparisons that can be made between the STORM9 and Parker simulations, given the presence of mean environmental horizontal vorticity and a cyclonically rotating updraft in the STORM9 simulation (the Parker simulation has no mean environmental horizontal vorticity or midlevel mesocyclone).

The presentation thus far has been merely descriptive. The sections that follow will answer these questions:

[5] M20 defined a TLV as a vortex having a 10-m ground-relative wind speed exceeding 29 m s^{-1} (lower threshold of EF0) and peak ζ exceeding either 0.25 s^{-1} at the scalar grid points (i.e., where p and θ_p are computed) or 0.50 s^{-1} at the ζ grid points (i.e., grid points halfway between the v grid points in the x direction and halfway between the u grid points in the y direction).

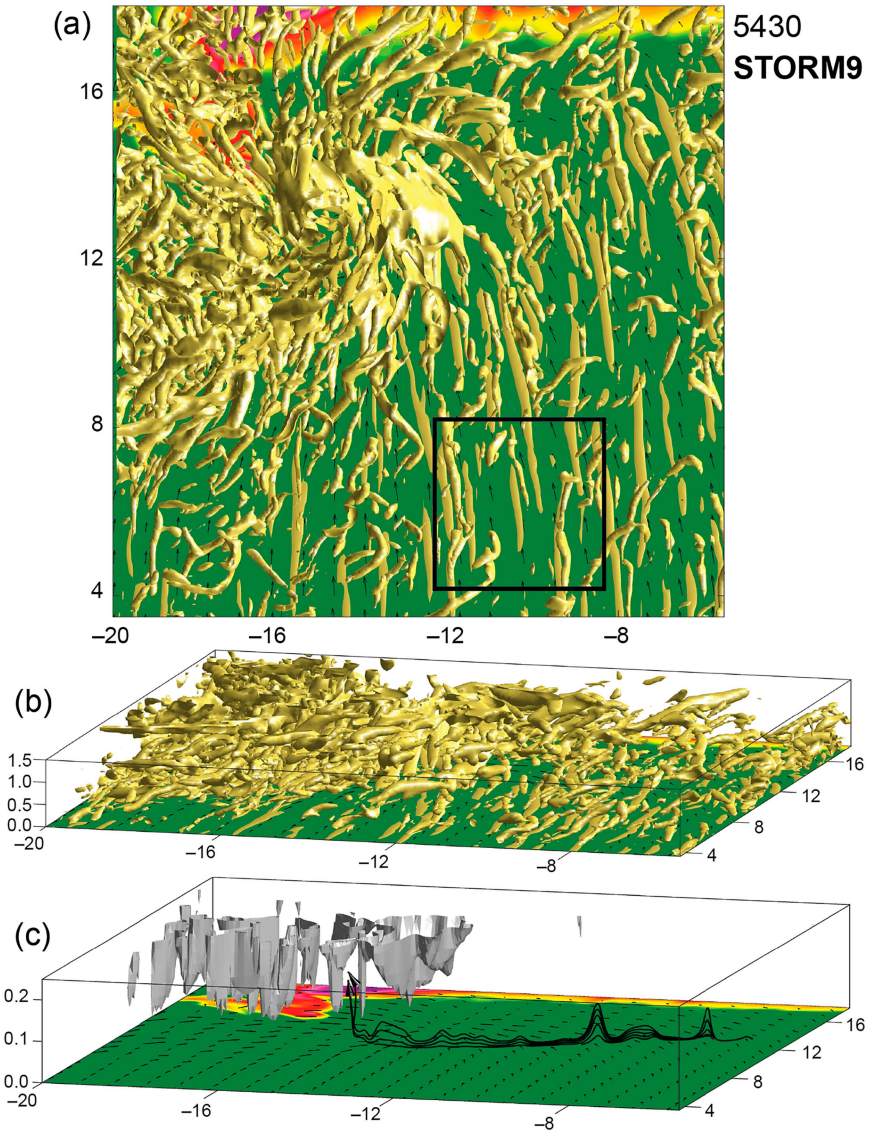

FIG. 7. (a) Depiction of the $\lambda_2 = -1 \times 10^{-4}$ s^{-2} isosurfaces in the STORM9 simulation at 5430 s, viewed from above, highlighting coherent structures in the boundary layer of the STORM9 simulation. The reflectivity field at $z = 7.5$ m is also displayed. The 4 km × 4 km black square encloses the region shown in Figs. 6a and 6b. Axis labels are in kilometers. (b) As in (a), but the view is from the southeast. (c) Zoomed-in view of the $w = 3$ m s^{-1} isosurface and near-surface vortex lines passing through $(x, y) = (-9, 12)$ at $z = 7.5$, 12.5, 17.5, 22.5, and 27.5 m.

1) What is the origin of the near-surface ζ streaks in the environmental air mass that appear to play a key role in TLV genesis?
2) How does the TLV end up on the cool side of the gust front (i.e., in its classic position) if the TLV originates from a positive-ζ anomaly in the environmental air?
3) What air feeds the developing TLV versus the mature TLV?
4) What is the origin of circulation for the TLV during its genesis phase, and is it any different once a mature TLV is established?
5) How can answers to the questions above be reconciled with the existing understanding of tornado formation, which has been derived from over a half century of observations, theory, and simulations?

c. *The characteristics and origin of near-surface ζ streaks*

Surface layers are well known in the atmospheric boundary layer and turbulence communities to be characterized by velocity streaks aligned with the ground-relative mean wind, with faster horizontal speeds in downdrafts and slower horizontal speeds in updrafts (e.g., Robinson 1991;

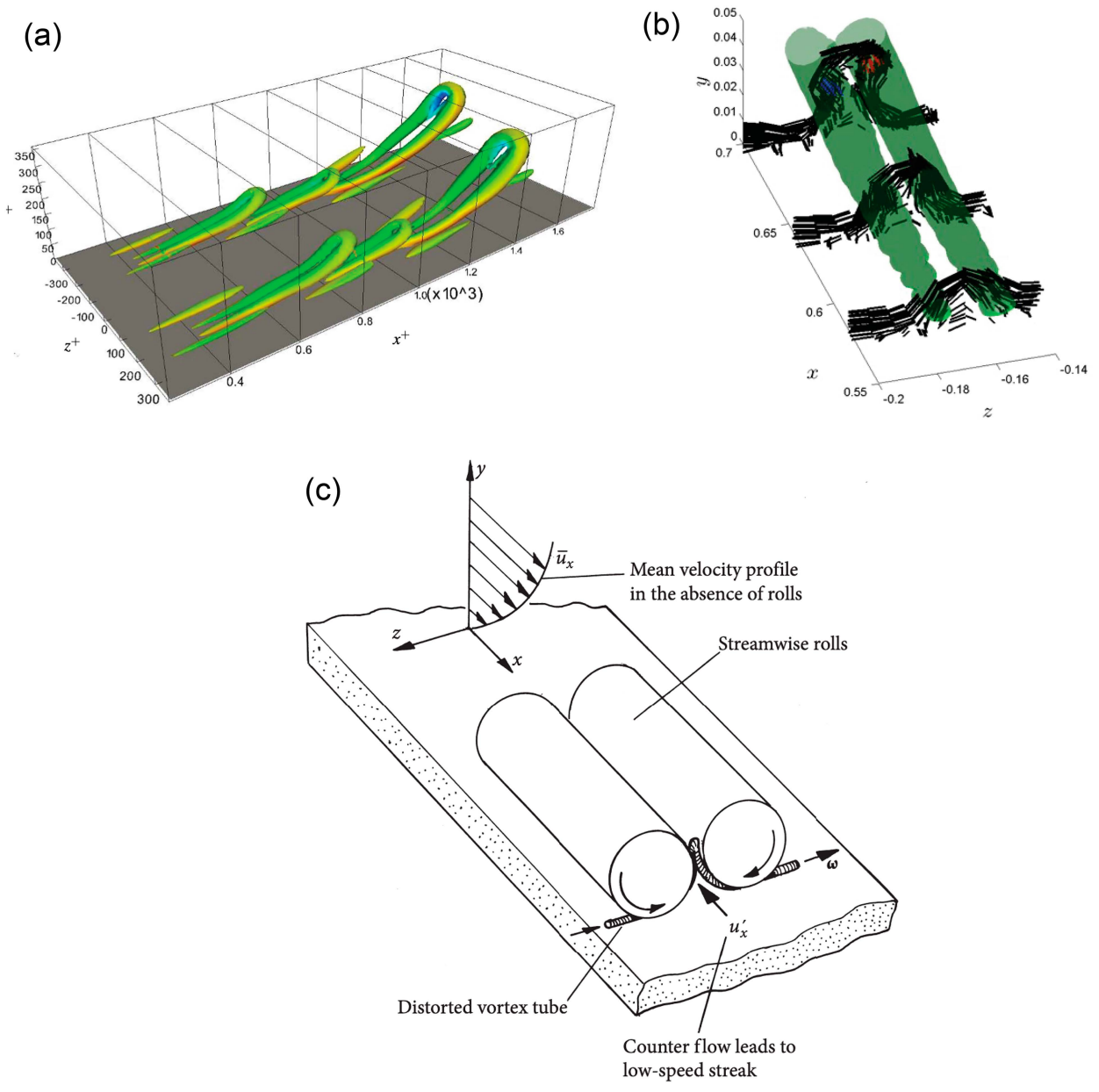

FIG. 8. Samples of visualizations of hairpin vortices and other coherent structures found in the literature. (a) Hairpin vortices in a channel flow, depicted via isosurfaces of 50% of the minimum λ_2 value, as simulated by Eitel-Amor et al. (2015). Axis labels indicate nondimensional distances. The flow direction is parallel to the x^+ axis. The Reynolds number is 590. (b) A pair of counterrotating, coherent (and vortical) structures (green isosurfaces) and accompanying vortex filaments (black) in a simulation by Bernard (2011). (c) Coherent structures in the surface layer as envisioned by Davidson (2015, p. 136), with an attendant vortex line.

Khanna and Brasseur 1998; Young et al. 2002), as is evident in the M20 simulations (Figs. 6a,b). In the M20 simulations, the ground-relative winds in the surface layer (nominally the lowest ~100 m AGL) are from 175° (i.e., approximately due south; Fig. 1). The horizontal wind speed streaks likewise imply the presence of ζ streaks a quarter wavelength out of phase with the horizontal wind speed streaks.

The surface-layer vortex lines tend to point approximately 90° to the left of the ground-relative wind, i.e., generally toward the west in the M20 environment. Thus, the ζ streaks, which are approximately orthogonal to the vortex lines, imply the presence of vortex-line corrugations in the vertical; i.e., the vortex lines are not purely horizontal, but rather have small vertical ripples along them owing to the tilting of horizontal vorticity by the horizontal gradients of vertical velocity (w; Figs. 6c and 7c). Small corrugations in the vortex lines in the horizontal plane are also present, owing to the cross-vortex-line wind speed variations associated with the horizontal velocity streaks, but the

focus is on the small-scale ζ anomalies owing to their potential to serve as "seeds" for TLV genesis.

The aforementioned longitudinal streaks of horizontal wind speed, w, and ζ are associated with what have been termed *coherent structures* or *eddies* in the boundary layer and turbulence communities (Alfonsi 2006; Adrian 2007; Bernard 2015). In a vertical plane oriented orthogonal to the longitudinal streaks (i.e., one oriented approximately west to east), the coherent structures take the form of horizontal vortices with alternating polarity (blue streamlines in Fig. 6c). A popular means of identifying coherent structures is via isosurfaces of the second eigenvalue of the matrix formed from the sum of the squares of the rate-of-strain and rotation tensors (λ_2), which is negative in a vortex core (Jeong and Hussain 1995; Alfonsi 2006; Adrian 2007; Bernard 2011, 2015; Eitel-Amor et al. 2015). The λ_2 parameter can be viewed as a three-dimensional extension of the Okubo–Weiss number (Okubo 1970; Weiss 1991), which might be more familiar to atmospheric scientists, many of whom use the latter to identify vortices (e.g., Markowski et al. 2011).

Isosurfaces of λ_2 are often misinterpreted as vortex tubes (Bernard 2011, 2019). However, λ_2 isosurfaces merely reveal where large curvature vorticity is present, whereas vortex lines are field lines for the full vorticity field (shear vorticity plus curvature vorticity). Near the surface in windy conditions, as in the M20 environment, shear vorticity directed to the left of the ground-relative wind, owing to southerly winds that increase rapidly in speed with height, is typically much larger than the curvature vorticity associated with eddies aligned with the ground-relative wind. Indeed, in the M20 environment, the mean horizontal vorticity (and vortex lines) points toward the west, and the λ_2 isosurfaces (roughly aligned with the southerly winds) are roughly orthogonal to the vortex lines (Figs. 7a,c). The vortex-line orientation and structure have some resemblance to the vortex lines computed from simulations by Moin and Kim (1985, see their Fig. 15) and Bernard (2011; Fig. 8b), and envisioned by Davidson (2015; Fig. 8c).

Perhaps the most studied coherent structures are what have been termed *hairpin vortices* (Fig. 8a). First envisioned by Theodorsen (1952, 1955), hairpin vortices have been studied by a long list of investigators spanning the boundary layer and turbulence communities (e.g., Moin and Kim 1985; Alfonsi 2006; Adrian 2007; Bernard 2011, 2015; Eitel-Amor et al. 2015). A lengthy review is beyond the scope of this article, but the interested reader might want to start with the textbook review by Davidson (2015, 134–139). It is difficult to find classic hairpin-like structures in the λ_2 isosurfaces in the surface layer of the M20 environment (Figs. 7a,b). In some parts of the domain, occasionally "wisps" of λ_2 isosurface structures resembling hairpins can be found, but mostly only the "legs" of hairpins are obvious. More classic hairpins in the λ_2 isosurfaces seem to be favored at lower Reynolds numbers than would characterize the M20 simulations (Fig. 8a). Regardless of whether or not the coherent structures in the M20 simulations should be regarded as hairpin vortices, legs of hairpins, or something else, what can be said definitively—and addresses the first question posed at the end of section 2b—is that coherent structures in the turbulent storm environment are responsible for the longitudinal horizontal velocity streaks, ζ streaks, and vortex-line corrugations (Figs. 7b,c and 8b,c).

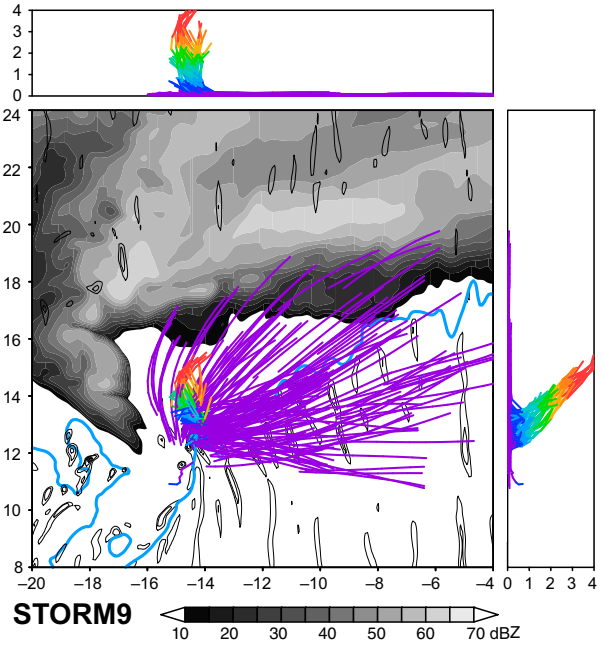

FIG. 9. Trajectories of parcels feeding the low-level mesocyclone in the STORM9 simulation in the minutes preceding tornadogenesis. Parcels that attain $\zeta \geq 0.05$ s^{-1} and $w \geq 5$ m s^{-1} below $z = 200$ m in the 5400–6000-s window are plotted from 5400 s (the time that parcels are introduced into CM1) until 5640 s (extending trajectories through 6000 s or beyond greatly reduces the visibility of the trajectories at low altitudes). Gust fronts, reflectivity (gray shading), and vertical vorticity at $z = 7.5$ m (0.01, 0.02, 0.04, 0.06 s^{-1}, etc.) at 5640 s are also displayed. Parcels that dip below $z = 7.5$ m at any point in their journey are excluded. The colors of the trajectories vary with altitude. Axis labels are in kilometers.

d. *Trajectories and vortex lines*

At 5400 s in the STORM9 simulation, 12.8 million parcels were inserted ahead of the storm, upstream of the incipient TLV, every 75 m in the x and y directions and every 25 m in the z direction, within the volume that spans $-16 < x < 14$ km, $2 < y < 32$ km, and 7.5 m $< z < 2$ km. The parcels track the resolved flow (i.e., the velocity interpolated to them is not modified with the SGS turbulent velocity) and are advanced every large model time step. Each parcel's coordinates, velocity components, and vorticity components are saved every 30 s (this is admittedly sparse sampling, but was sufficient for the purposes of this study and, given the adaptive time step, ensured a rerun simulation that closely matched M20's STORM9 simulation). Parcels that dip below the lowest grid level for horizontal velocity ($z = 7.5$ m) at any point in their journey are excluded from the analysis.

In the pretornadic period (i.e., prior to 6250 s), a broad envelope of parcels feeds the low-level mesocyclone from both sides of the forward-flank gust front (Fig. 9), though the parcels on the cool side of the gust front are generally no more

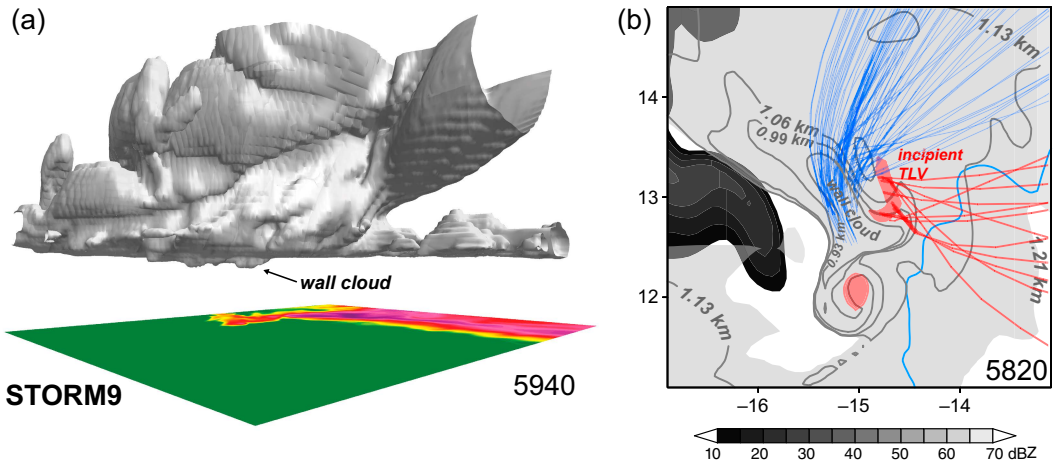

FIG. 10. (a) View from the southeast of the 0.1 g kg^{-1} cloud water isosurface at 5940 s in the STORM9 simulation. Reflectivity at $z = 7.5$ m is also displayed (color shading). (b) Horizontal cross section depicting the wall cloud and incipient TLV region at 5820 s. Light gray shading indicates where cloud is present (cloud water > 0.1 g kg^{-1}) at $z = 1.21$ km. Gray contours enclose cloudy regions at $z = 1.13$, 1.06, 0.99, and 0.93 km. Red shading indicates $\zeta \geq 0.1$ s^{-1} at $z = 0.93$ km. Trajectories into the wall cloud (blue) and incipient TLV (red) are shown (both sets of trajectories pass within 20 m of the $z = 0.93$ grid level in the wall cloud and incipient TLV regions). Reflectivity ($z = 7.5$ m) also is displayed on the bottom layer of the figure (gray shading according to the legend), as is the $\theta'_\rho = -0.25$-K isopleth ($z = 7.5$ m), which serves as a gust-front proxy.

than 1 K cooler (and slightly more humid) than those entering the low-level mesocyclone from the environment to the south of the gust front. As a result, the storm's wall cloud (Fujita 1960; Lemon and Doswell 1979; Doswell and Burgess 1993) is rather modest, characterized by a cloud base only ~300 m lower than the ambient cloud base (Fig. 10).

However, a closer inspection of the trajectories reveals that the parcels that enter the developing TLV during the axisymmetrization period (5640–6000 s), as opposed to parcels that merely enter the low-level mesocyclone, originate *solely in the environment* (Fig. 11a). Some of the environmental parcels have significant ζ prior to reaching the incipient TLV owing to the vortex-line corrugations produced by the eddies described above. Perhaps surprisingly, the magnitude of the horizontal vorticity of these parcels (~0.10–0.35 s^{-1}) exceeds that of the parcels on the cool side of the gust front where baroclinicity is present (~0.03–0.05 s^{-1}). Near-surface horizontal vorticity in the forward-flank baroclinic zone is reduced relative to the environment because of the combination of the lower boundary condition and a deceleration of the southerly ground-relative winds within the forward-flank precipitation region (the northward-moving parcels encounter an adverse horizontal pressure gradient force owing to the high pressure perturbation associated with the cool outflow). Because of surface drag, near-surface horizontal vorticity is mostly a function of the near-surface wind speed,[6] so slower speeds result in diminished near-surface horizontal vorticity, despite the presence of baroclinic horizontal vorticity generation on the southern edge of the storm's forward-flank precipitation region.

Parcels from the cool side of the gust front only enter the TLV *once the TLV has formed* (Figs. 11b–d). At that point, parcels are drawn into the TLV from practically all directions. As for the wall cloud, unsurprisingly it is fed by trajectories originating on the cool side of the gust front; however, the pocket of amplifying ζ associated with the incipient TLV lies slightly east of the cloud lowering (Fig. 10b).

Given the near-conservation of θ_ρ along the portion of the gust front that lies in the vicinity of TLV genesis (this region lacks hydrometeors), the gust front in the TLV genesis region ought to be a material boundary. The curious reader will therefore surely wonder how the ζ maximum ends up on the cool side of the gust front (Figs. 4b–f)—i.e., its classic position—if it is the result of the amplification of ζ within parcels in the environment. The answer lies in the forcings for $\partial\zeta/\partial t$ and $\partial\theta/\partial t$ from the SGS turbulence parameterization. Figure 12 provides a close-up perspective of the positive-ζ anomaly associated with TLV genesis (the one labeled "m" in Fig. 5) as it approaches the gust front from 5760 to 5820 s, and subsequently migrates through the airmass boundary from 5850 to 5880 s, arriving in the classic final position in the cool air, with outflow wrapped around it, by 5970 s, mere minutes before TLV status is attained. The forcing for $\partial\zeta/\partial t$ from the SGS turbulence parameterization has a dipole structure that straddles the ζ maximum, with $\partial\zeta/\partial t > 0$ (<0) on the western (eastern) flank of the ζ maximum, thereby implying a westward propagation of the ζ maximum (i.e., toward the cool side of the gust front) (Figs. 12d–h). At the same time, a

[6] For example, at the lowest scalar level ($z_1 = 7.5$ m), the semi-slip lower boundary condition implies a horizontal vorticity magnitude of $|\boldsymbol{\omega}_h| = M_1[z_1 \ln(z_1/z_0)]^{-1} \approx 0.03M_1$, where M_1 is the ground-relative wind speed at z_1 and z_0 (=0.12 m) is the roughness length.

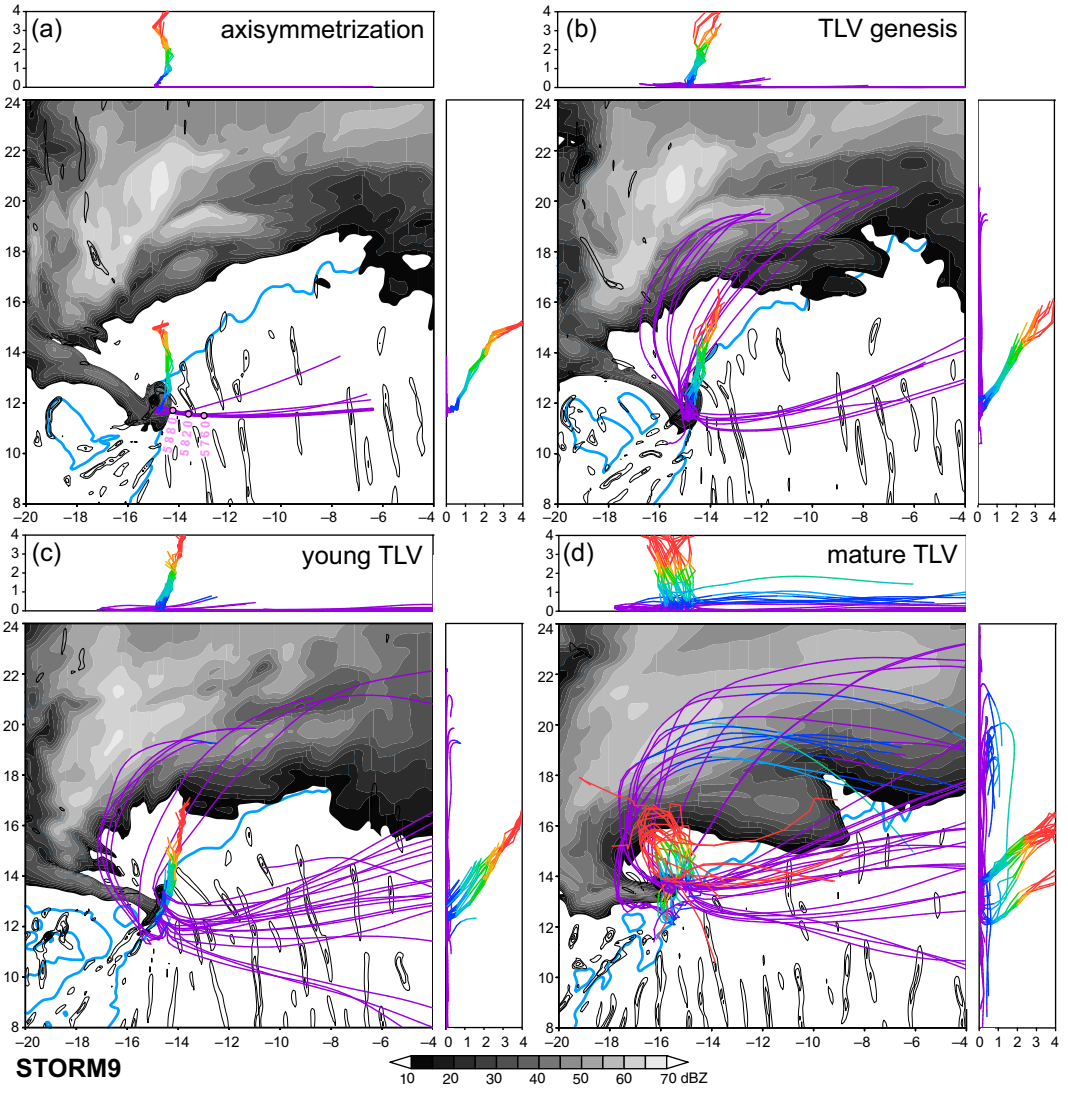

FIG. 11. Trajectories of parcels that attain $\zeta \geq 0.05\ s^{-1}$ below $z = 22.5$ m (the second grid level for ζ) in the STORM9 simulation during the (a) "axisymmetrization" period (5640–6000 s), (b) "TLV genesis" period (6000–6250 s), (c) "young TLV" period (6250–6600 s), and (d) "mature TLV" period (6600–7200 s). Trajectories are plotted from 5400 s (the time that parcels are introduced into CM1) until 6270, 6360, 6600, and 7200 s in the respective panels; gust fronts, reflectivity (gray shading), and vertical vorticity at $z = 7.5$ m (0.01, 0.02, 0.04, 0.06, …, 0.40 s^{-1}) are also displayed in each panel at these times. Parcels that dip below $z = 7.5$ m at any point in their journey are excluded. The colors of the trajectories vary with altitude. Axis labels are in kilometers. The parcel in (a) whose trajectory has a broader line width is the one showcased in Fig. 13. The locations of the parcel at 5760, 5820, and 5880 s are also indicated.

region of $\partial\theta/\partial t < 0$ from the SGS turbulence parameterization is present along, and extends slightly ahead of, the gust front in the vicinity of the ζ maximum, thereby implying an eastward propagation of the gust front owing to the SGS $\partial\theta/\partial t$ forcing (Figs. 12d–h). In summary, both westward propagation of the ζ maximum and eastward propagation of the gust front, both driven by their respective SGS turbulence forcings, promote the migration of the intensifying ζ maximum from the warm side of the gust front to the cold side.

The evolution of the vortex lines that pass through a representative air parcel that feeds the incipient TLV is shown in Fig. 13 (this parcel's trajectory is emboldened in Fig. 11a). Though it is tempting to regard the depictions as being that of the same vortex line owing to the lack of baroclinicity along the parcel's trajectory (according to Helmholtz's theorem, one requirement for a vortex line to behave as a material line is for baroclinicity to be absent), the presence of SGS mixing within the parcel would preclude the vortex lines drawn through a single parcel at multiple times from being strictly interpreted as the same vortex line at each time (the second requirement of Helmholtz's theorem is inviscid flow). Nonetheless, the evolution of the vortex lines through the parcel bound for the

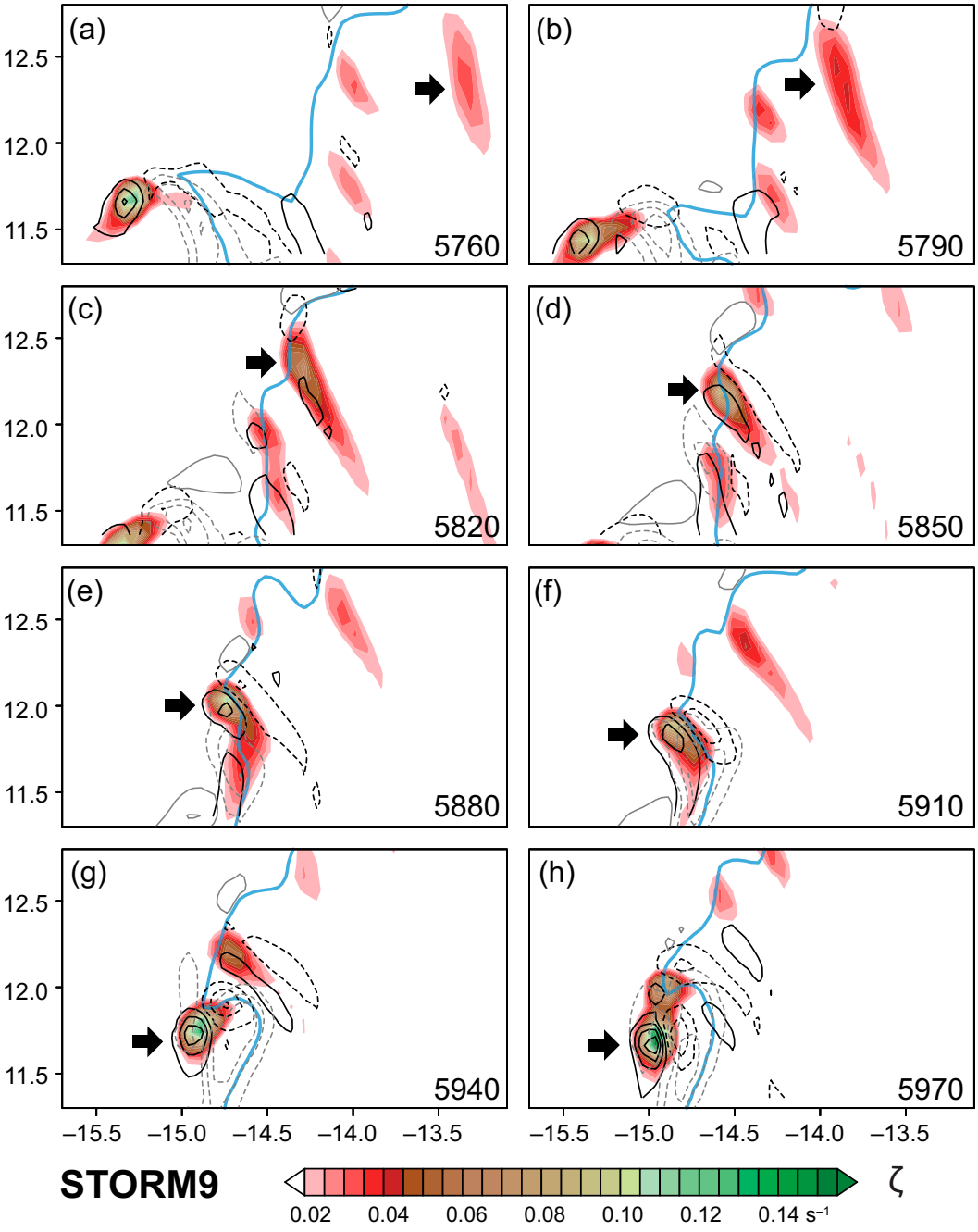

FIG. 12. Horizontal cross sections of ζ at $z = 7.5$ m (shaded) in the STORM9 simulation, with contributions to $\partial\zeta/\partial t$ and $\partial\theta/\partial t$ from the SGS turbulence parameterization, from (a) 5760 to (h) 5970 s at 30-s intervals. The contribution to $\partial\zeta/\partial t$ from the SGS turbulence parameterization is contoured with black isopleths every 0.0004 s^{-2}, starting at -0.0010 s^{-2}, with negative values indicated with dashed contours (i.e., -0.0010, -0.0006, -0.0002, 0.0002, 0.0004 s^{-2}, etc.). The contribution to $\partial\theta/\partial t$ from the SGS turbulence parameterization is contoured with gray isopleths every 0.01 K s^{-1}, starting at -0.035 K s^{-1}, with negative values indicated with dashed contours (i.e., -0.035, -0.025, -0.015, -0.005, 0.005 K s^{-1}, etc.). The $\theta'_\rho = -0.25$ K isopleth (broad cyan contours) is overlaid to serve as a proxy for the gust-front location. Axis labels are in kilometers. The black arrow in each panel identifies the ζ maximum that ultimately attains TLV status at 6240 s.

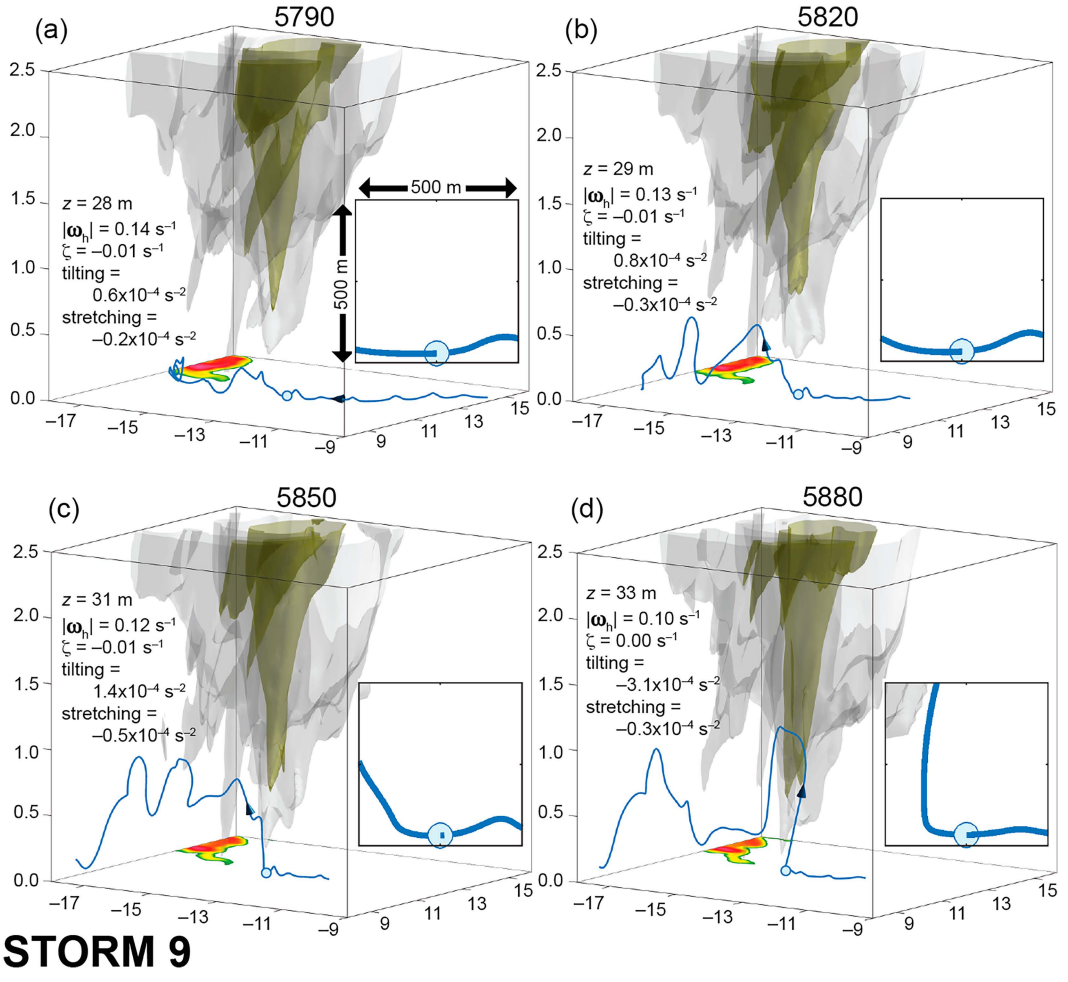

FIG. 13. Vortex line drawn through an air parcel that approaches and eventually enters the developing TLV in the STORM9 simulation (this parcel's trajectory is emboldened in Fig. 11a). The vortex line is terminated where it dips below $z = 15$ m (the lowest grid level where centered-difference estimates of the horizontal vorticity are available). The $w = 10$ and 20 m s^{-1} isosurfaces and reflectivity at $z = 7.5$ m also are displayed. Axis labels are in kilometers. The inset of each panel shows a close-up view of the parcel and vortex line as viewed from the south in a 500 m × 500 m x–z vertical cross section that has the same horizontal and vertical scales (the vertical axes are stretched in the main windows). The parcel's altitude, horizontal vorticity magnitude ($|\boldsymbol{\omega}_h|$), ζ, and its tilting and stretching ζ tendencies also are displayed at each time. The location of the parcel at 6000 s is shown in Fig. 14c–e.

incipient TLV is unlikely to be wildly different than the evolution of a single vortex line in this region.

At 5790 s, the vortex line is quasi horizontal, but with corrugations as discussed in section 2c (Fig. 13a). (In addition to excluding parcels from analysis that dip below the first u–v grid level at $z = 7.5$ m at any point in their histories, vortex lines are terminated where they dip below $z = 15$ m, which is the lowest grid level where centered-difference estimates of the horizontal vorticity are available.) The vortex lines drawn through the parcel from 5820 to 5910 s (Figs. 13b–e) give the impression of vortex lines having been drawn upward by the overlying supercell storm's updraft. By 5940 s (Fig. 13f), the vortex lines drawn through the parcel connect with the midlevel mesocyclone of the supercell. Near the surface, the vortex lines bend almost 90° upward within the lowest 50 m (see insets in Figs. 13d–h). The parcel's ζ increases from -0.01 s^{-1} at 5910 s to 0.06 s^{-1} at 5940 s (Figs. 13f,g), and just 30 s later, ζ increases to 0.17 s^{-1} within the parcel as it rapidly rises away from the surface (Fig. 13h). A parcel with initially negative ζ was deliberately chosen to make the point that the finding of section 2b that positive-ζ anomalies serve as foci for TLV genesis (Figs. 5 and 12) does not imply that only parcels with initially positive ζ can feed the TLV.

Both large tilting [$\boldsymbol{\omega}_h \cdot \nabla_h w$, where $\boldsymbol{\omega}_h = (\partial w/\partial y - \partial v/\partial z)\mathbf{i} + (\partial u/\partial z - \partial w/\partial x)\mathbf{j}$ is the horizontal vorticity] and stretching [$(\zeta + f_0)\partial w/\partial z \approx \zeta\partial w/\partial z$, where $f_0 = 10^{-4}$ s^{-1} is the Coriolis parameter] play a role in the explosive growth of ζ and reorientation of vortex lines from quasi horizontal to vertical next to the surface, with instantaneous tilting and stretching peaking at 41.4×10^{-4} s^{-2} and 26.5×10^{-4} s^{-2}, respectively, at 5940 s

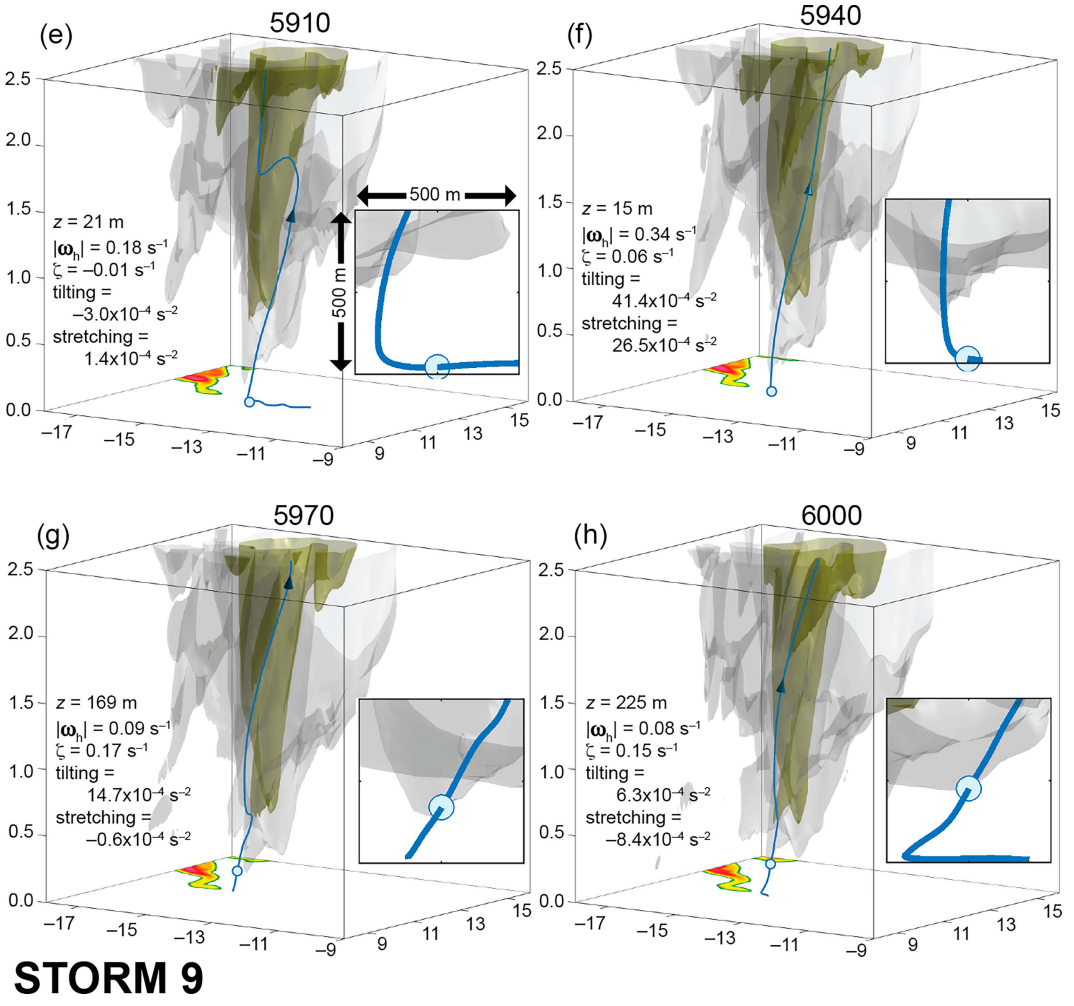

FIG. 13. (*Continued*)

(Fig. 13f). A parcel experiencing these forcings for 30 s would see its ζ increase by 0.2 s^{-1} in that time, neglecting the effects of turbulent diffusion. Moreover, this rapid growth of ζ, and reorientation of vortex lines from horizontal to vertical, occurs on the *environmental side* of the gust front (cf. Figs. 11a and 13a–f).

The Lagrangian perspective of the evolution of ζ and vortex lines within an air parcel approaching the developing TLV is complemented by horizontal cross sections of the tilting and stretching fields in Fig. 14, and a more holistic view of vortex lines (all vortex lines that pass through grid points within the high-ζ region at $z = 266$ m) in Fig. 15. The influence of longitudinal coherent turbulent eddies in the surface layer is apparent in the tilting and stretching fields, in the sense that approximately north–south-oriented extrema are present throughout the storm's environment, even into the far field (Figs. 14a,b). The magnitudes of both tilting and stretching increase in the vicinity of the storm's updraft region (Figs. 14c–e); tilting increases owing to increases in $|\boldsymbol{\omega}_h|$ in the near-storm inflow (to be discussed further in section 2e) and stretching increases owing to increases in both ζ and $\partial w/\partial z$. As explained in section 2b, the near-surface positive-ζ anomalies tend to be stronger than the negative-ζ anomalies, and this also implies a positive stretching bias (Fig. 14a). Closer to the storm updraft, storm-scale convergence acting on f_0 also contributes to both positive ζ and positive stretching biases (Fig. 14c).

Regarding the depiction of the vortex lines associated with the low-level mesocyclone region (Fig. 15), as was the case for the Lagrangian perspective (Fig. 13), the picture that emerges is that the overlying storm updraft draws environmental vortex lines upward in the TLV-genesis region, with vortex lines becoming quasi vertical in the environment beneath the eastern flank of the updraft at grid levels adjacent to the surface in the minutes preceding TLV formation. The negative-ζ anomalies vanish (i.e., vortex-line corrugations vanish) as vortex lines are drawn upward (Figs. 13c–g), owing to large positive tilting even within parcels initially possessing $\zeta < 0$. The horizontal vorticity is highly streamwise with respect to the storm-relative winds in the boundary layer, which are predominantly from the east given the storm motion toward the northeast (Fig. 1). Thus, when the vortex lines are drawn

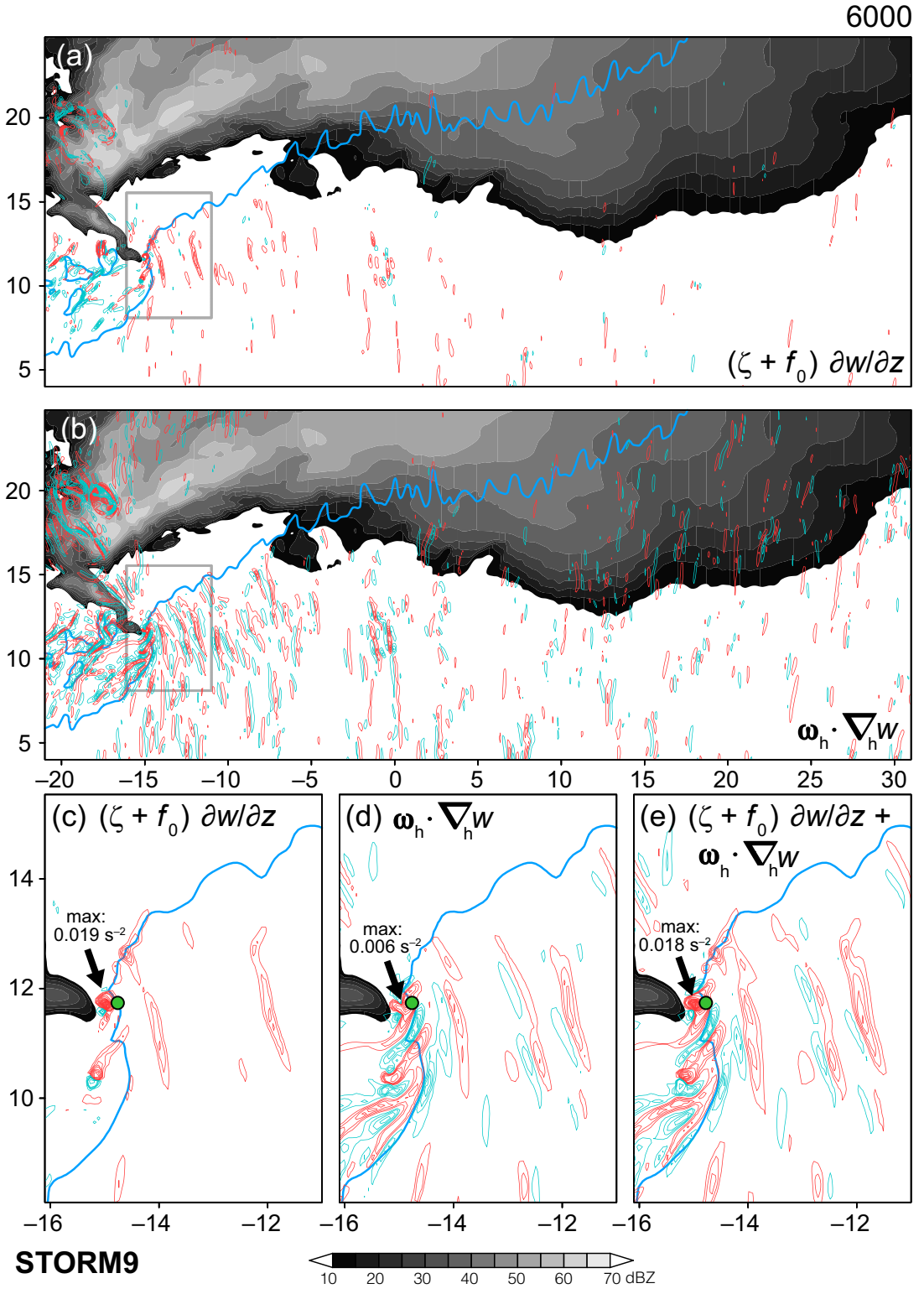

FIG. 14. Vertical vorticity (a) stretching and (b) tilting at $z = 15$ m at 6000 s in the STORM9 simulation. Positive (negative) isovorts are red (cyan); the contour levels are $\pm 1, 3, 5 \times 10^{-4}$ s^{-2}, etc. Reflectivity (gray shading) and the gust front ($\theta'_\rho = -0.25$ K isopleth) also are displayed. Axis labels are in kilometers. The gray rectangles indicate the region displayed in (c)–(e), which depict vertical vorticity stretching, tilting, and stretching + tilting, respectively. The contour levels in (c)–(e) are $\pm 2, 4, 6, 8, 10, 20, 30, \ldots, 190 \times 10^{-4}$ s^{-2}. The green shaded circle in (c)–(e) indicates the parcel referred to in Fig. 13.

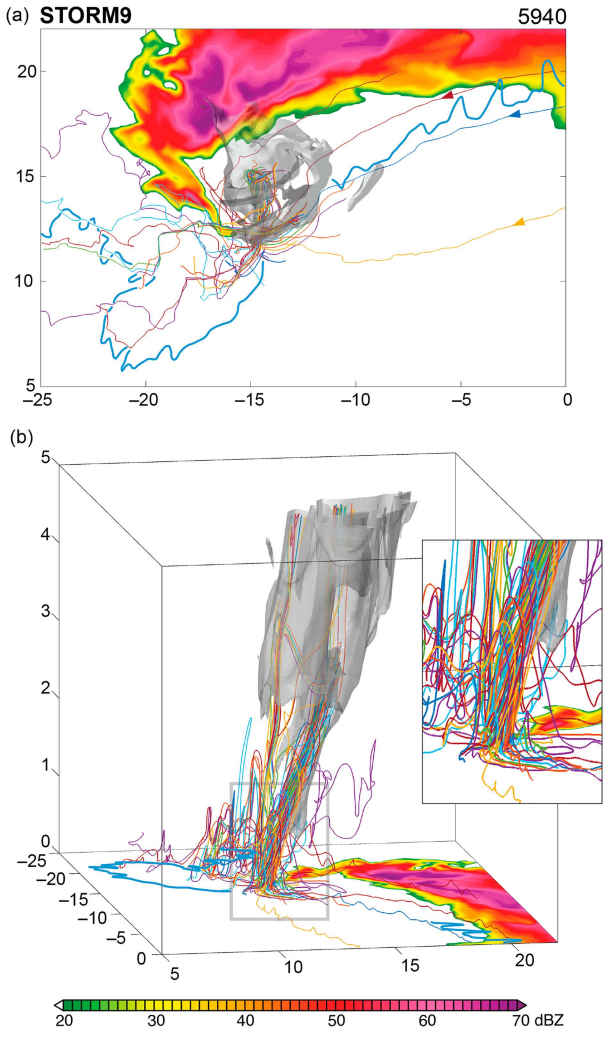

FIG. 15. Vortex lines in the STORM9 simulation at 5940 s, viewed from (a) above and (b) from the east-southeast. Each vortex line has a different color. The vortex lines all pass through grid points at which $\zeta \geq 0.05\ s^{-1}$ at $z = 266$ m. The $w = 20\ m\ s^{-1}$ isosurface (gray), reflectivity at $z = 7.5$ m (color shading), and gust front (thick blue contour) also are displayed. Axis labels are in kilometers. Vortex lines are terminated where they pass below $z = 15$ m (the lowest grid level where centered-difference estimates of the horizontal vorticity are available).

upward by the overlying storm updraft, the positive ζ ends up being collocated with large w and $\partial w/\partial z$ associated with the storm updraft (Davies-Jones 1984), which greatly benefits the further amplification of the positive ζ.

e. *Sources of circulation for the TLV*

1) OVERVIEW

Material circuit analyses were performed in order to quantify the sources of circulation for the TLV, both near the time of genesis, as well as during its maturity. Potentially these could be different, particularly because of the differences in trajectories before and after TLV formation, as documented in section 2d.

Material circuit analyses are a useful tool for diagnosing the various contributions to the circulation that can give rise to an intense vortex (e.g., Rotunno and Klemp 1985; Davies-Jones and Brooks 1993; Markowski and Richardson 2014b; Markowski 2016; Mashiko 2016; Roberts and Xue 2017; Tao and Tamura 2020). One advantage over vorticity budgets computed along individual trajectories is that the terms in the vorticity equation involve products of velocity derivatives, and are therefore more error prone than the line-integral calculations involved in a circulation analysis. Moreover, the trajectories into a TLV are themselves potentially error prone given the extreme accelerations encountered near or within an intense vortex. In material circuit analyses, typically a ring of parcels is tracked backward from an initial radius that avoids a vortex's most extreme accelerations. However, it might be preferable not to make the initial radius so large that a significant fraction of the parcels in the circuit never actually enters the TLV if their trajectories are extended forward in time (the author suspects that this probably has been the case in some past circulation analyses, which might partly explain the lack of consensus in past analyses). After all, if an investigator claims to be interested in the circulation giving rise to or maintaining the TLV or tornado, then it would seem that the entire circuit ought to eventually collapse upon the vortex.

The trajectories of the parcels comprising the circuits were computed backward in time using the 30-s model output and a fourth-order Runge–Kutta scheme with a time step of 10 s. Parcels that drop below $z = 7.5$ m have horizontal velocities extrapolated to them via second-order extrapolation using the horizontal velocities at the first three interior grid levels ($z = 7.5$, 22.5, and 37.5 m). The distance between adjacent parcels in the circuits is checked at each time step to ensure that the circuits remain well represented, lest the numerical calculation of the relative circulation about the circuit, $C = \oint \mathbf{v} \cdot d\mathbf{x}$ (where $\mathbf{v} = u\mathbf{i} + v\mathbf{j} + w\mathbf{k}$ is the three-dimensional velocity and $\mathbf{x} = x\mathbf{i} + y\mathbf{j} + z\mathbf{k}$ is the position vector) is unreliable. Parcels inevitably diverge from one another as they are advanced backward in time, given that the ζ maxima initially encircled by the circuits form within strongly confluent horizontal flow. Additional parcels are inserted each time step, as needed, so that there are never more than 25 m between adjacent parcels. The circuits analyzed below contain 10 000 parcels at the time they are introduced, but this number typically grows by a factor of 3–5 by the time a 40-min backward integration has been carried out.

Each material circuit's C is governed by Bjerknes's circulation theorem,

$$\frac{dC}{dt} = \oint \alpha\, dp \; - \oint (f_0 \mathbf{k} \times \mathbf{v}_h) \cdot d\mathbf{x} + \oint \mathbf{F} \cdot d\mathbf{x} + \oint \mathbf{K} \cdot d\mathbf{x}, \quad (1)$$

where α is the specific volume of air, p is pressure, $\mathbf{v}_h$ is the horizontal velocity, $\mathbf{F}$ represents the accelerations from SGS turbulence ($\mathbf{F}_{\text{SGSTURB}}$) and numerical diffusion ($\mathbf{F}_{\text{DIFFUSION}}$), and $\mathbf{K}$ is the Davies-Jones (2021) invented force (see appendix B). The diagnosed relative circulation of the circuits is obtained by integrating (1), i.e.,

$$C_{\text{DIAGNOSED}}(t) = C_0 + C_{\text{BAROCLINIC}} + C_{\text{SGSTURB}} + C_{\text{DIFFUSION}} + C_{\text{CORIOLIS}} + C_{\text{INVENTED}}, \quad (2)$$

where

$$C_{\text{BAROCLINIC}}(t) = -\int\oint \alpha \, dp \, dt \approx -\int\oint B \, dz \, dt, \quad (3)$$

$$C_{\text{SGSTURB}}(t) = \int\oint \mathbf{F}_{\text{SGSTURB}} \cdot d\mathbf{x} \, dt, \quad (4)$$

$$C_{\text{DIFFUSION}}(t) = \int\oint \mathbf{F}_{\text{DIFFUSION}} \cdot d\mathbf{x} \, dt, \quad (5)$$

$$C_{\text{CORIOLIS}}(t) = -\int\oint (f_0\mathbf{k} \times \mathbf{v}_h) \cdot d\mathbf{x} \, dt, \quad (6)$$

$$C_{\text{INVENTED}}(t) = \int\oint \mathbf{K} \cdot d\mathbf{x} \, dt, \quad (7)$$

where $B = -g\theta_\rho'/\bar{\theta}_\rho$ is the buoyancy, and $C_{\text{BAROCLINIC}}$, C_{SGSTURB}, $C_{\text{DIFFUSION}}$, C_{CORIOLIS}, and C_{INVENTED} represent, respectively, the partial circulations from baroclinicity, the SGS turbulence parameterization, numerical diffusion, the Coriolis acceleration, and the invented force.

The integrations are carried out backward in time, but to ease the interpretation of the budgets presented in Figs. 16 and 17 (the author prefers to interpret such graphs going forward in time), the partial circulations are set to 0 at the beginning of the time periods analyzed, and C_0 represents the circulation at that time (as opposed to representing the circulation at the end of the time window, which is the starting point of the backward-in-time integration). If the circuit is in the storm environment by the time the backward integration is completed, C_0 can be regarded as the barotropic circulation (i.e., circulation associated with the barotropic vorticity; Dutton 1986, p. 390; Davies-Jones et al. 2001; Markowski 2016; Davies-Jones and Markowski 2021).

Although it might seem as though 30-s output are rather coarse for performing analyses of this sort, the circulation budgets are fairly well reconciled even going as far backward in time as 40 min. In other words, the instantaneous C obtained from $\oint \mathbf{v} \cdot d\mathbf{x}$ tends to be in relatively good agreement with the circulation diagnosed from (2). As the circuits go backward in time in high-resolution simulations, especially simulations with a turbulent environment, circuits unavoidably get extremely contorted (one colleague has referred to them as "piles of lunchmeat").[7] A circuit that initially surrounds a vortex may develop folds as the circuit is advanced backward in time, owing to the fact that individual parcels comprising the circuit may orbit the vortex a different number of times before escaping. Although one cannot practically envision a flux of vortex lines through a surface defined by such a complex circuit (from Stokes's theorem, circulation is proportional to the flux of vortex lines through the surface defined by the circuit), the circulation budget calculations given by (2)–(7) are agnostic about the complexity of the circuit and still provide a reliable assessment of the various contributions to the total circulation (the circulation budgets essentially represent the aggregate vorticity budgets of a large number of trajectories).

2) "EARLY" MATERIAL CIRCUIT ANALYSES: 3540–5940 S

The first material circuit analyzed is introduced at 5940 s, during the axisymmetrization period (Table 1), approximately a minute prior to TLV genesis (Fig. 16). The circuit has a radius of 500 m and encircles the ζ maximum associated with the incipient TLV. The circuit is placed at $z = 15$ m, which reduces the number of parcels that drop below the lowest scalar grid level compared with a circuit introduced at $z = 7.5$ m. The circuit is tracked 40 min (2400 s) backward in time, by which point it is outside of the presupercellular storm (Fig. 16a). The circuit's C at 5940 s is a rather modest 10 000 $\text{m}^2\,\text{s}^{-1}$ (Fig. 16e), which should be regarded as being close to the bare minimum required to yield EF0 (ground-relative) winds upon being contracted to a radius of $\approx 2\Delta x = 150$ m.[8]

The analysis of the partial circulations of the circuit (Fig. 16e) at 5940 s reveals that ≈70% of $C_{\text{DIAGNOSED}}$ is attributable to C_0 and ≈30% is attributable to C_{SGSTURB} at that time. However, over roughly the first half of the circuit's journey toward the TLV, SGS turbulence destroys practically all of the initial circulation. The circulation recovers to its value of 10 000 $\text{m}^2\,\text{s}^{-1}$ at 5940 s as a result of circulation generation by SGS turbulence forcing, with the net SGS turbulence forcing being positive over the entire journey. On one hand, without C_0 there would not be enough circulation for a TLV (C_{SGSTURB} is not nearly large enough to yield TLV-strength tangential velocities). On the other hand, the positive C_{SGSTURB} generated in the latter half of the integration (4740–4940 s) is significant, and accounts for nearly all of the positive circulation acquired by the circuit once its circulation had been destroyed by turbulence. The influence of surface drag on circulation generation *during the circuit's analysis window* would be baked into C_{SGSTURB}; however, surface drag also contributes to C_0 by virtue of the fact that the strong low-level wind shear in the environment at the time of convection initiation is the principally the result of surface drag.

The circulation contributions from baroclinicity, the Coriolis force, numerical diffusion, and the invented force are all negligible (Fig. 16e). The lack of a significant role for baroclinic generation of circulation is particularly

[7] The supplementary material contains animations depicting the evolution of the material circuits.

[8] The storm motion is toward the northeast at 17.4 m s^{-1}, so a vortex tangential velocity (v_θ) of 11.6 m s^{-1} would be needed to reach the 29 m s^{-1} EF0 threshold. For $C = 10\,000$ $\text{m}^2\,\text{s}^{-1}$ and $v_\theta = 11.6$ m s^{-1}, $r = C/2\pi v_\theta = 137$ m $\sim 2\Delta x$.

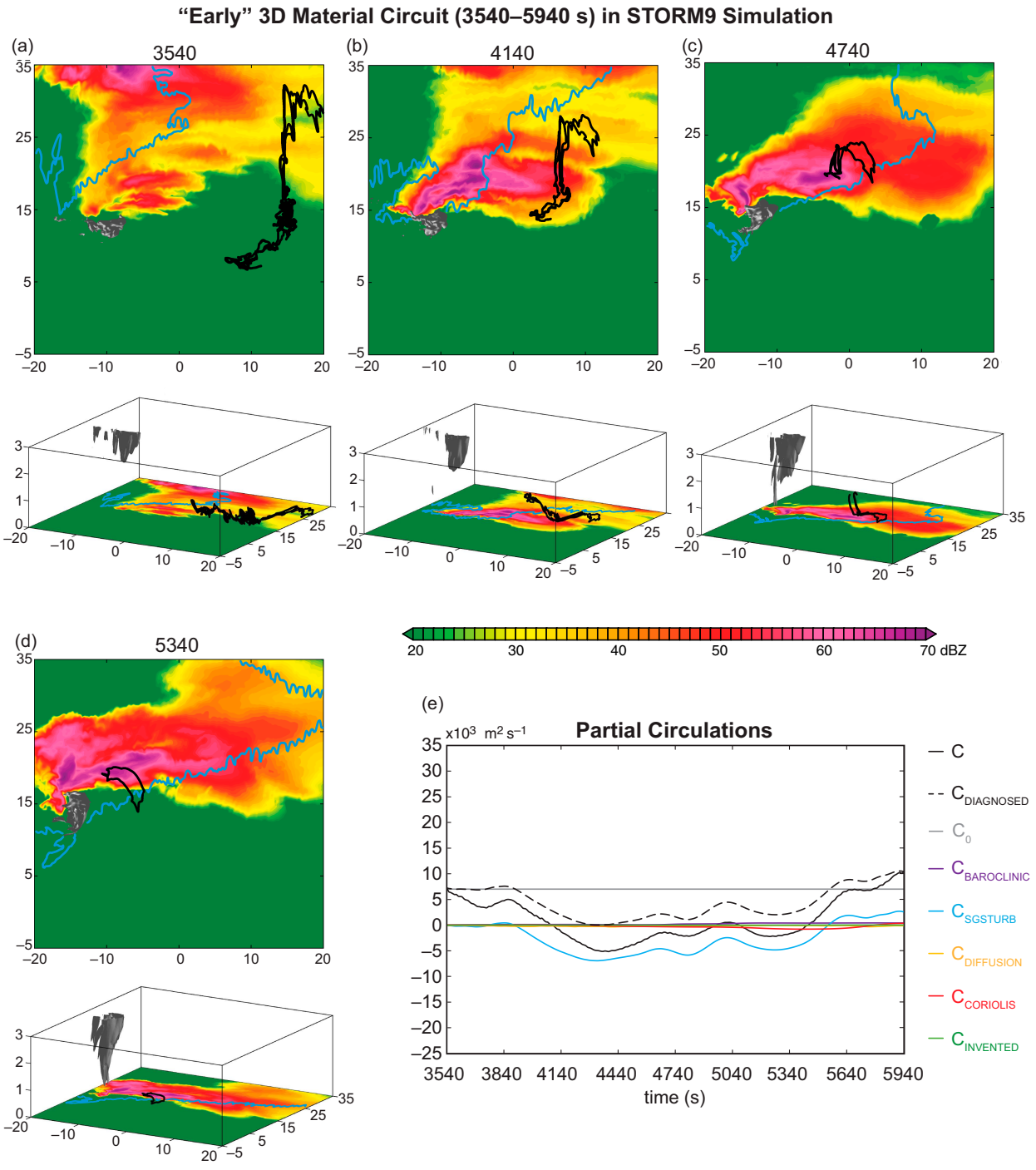

FIG. 16. Analysis of a material circuit tracked from 3540 to 5940 s in the STORM9 simulation. (a)–(d) Views of the circuit from above and from the southeast at 600-s intervals from 3540 to 5340 s. At 5940 s, the circuit is a circle with a radius of 0.5 km located in the horizontal plane at $z = 15$ m. The circuit is plotted above the simulated reflectivity field at the lowest model level. The 15 m s^{-1} vertical velocity isosurface is also displayed, as is the $\theta'_\rho = -0.25$ K isopleth (bold blue contours). The latter serves as a proxy for the gust-front location. Axis labels are in kilometers. (e) Partial circulations of the material circuit. See text for further details.

noteworthy, given the large volume of prior numerical studies that have found it to be the dominant means by which near-surface ζ develops in supercells (e.g., Rotunno and Klemp 1985; Davies-Jones and Brooks 1993; Adlerman et al. 1999; Dahl et al. 2014; Markowski and Richardson 2014b; Dahl 2015).

Although introducing the circuit at $z = 15$ m reduces the fraction of the circuit that dips below the lowest scalar level,

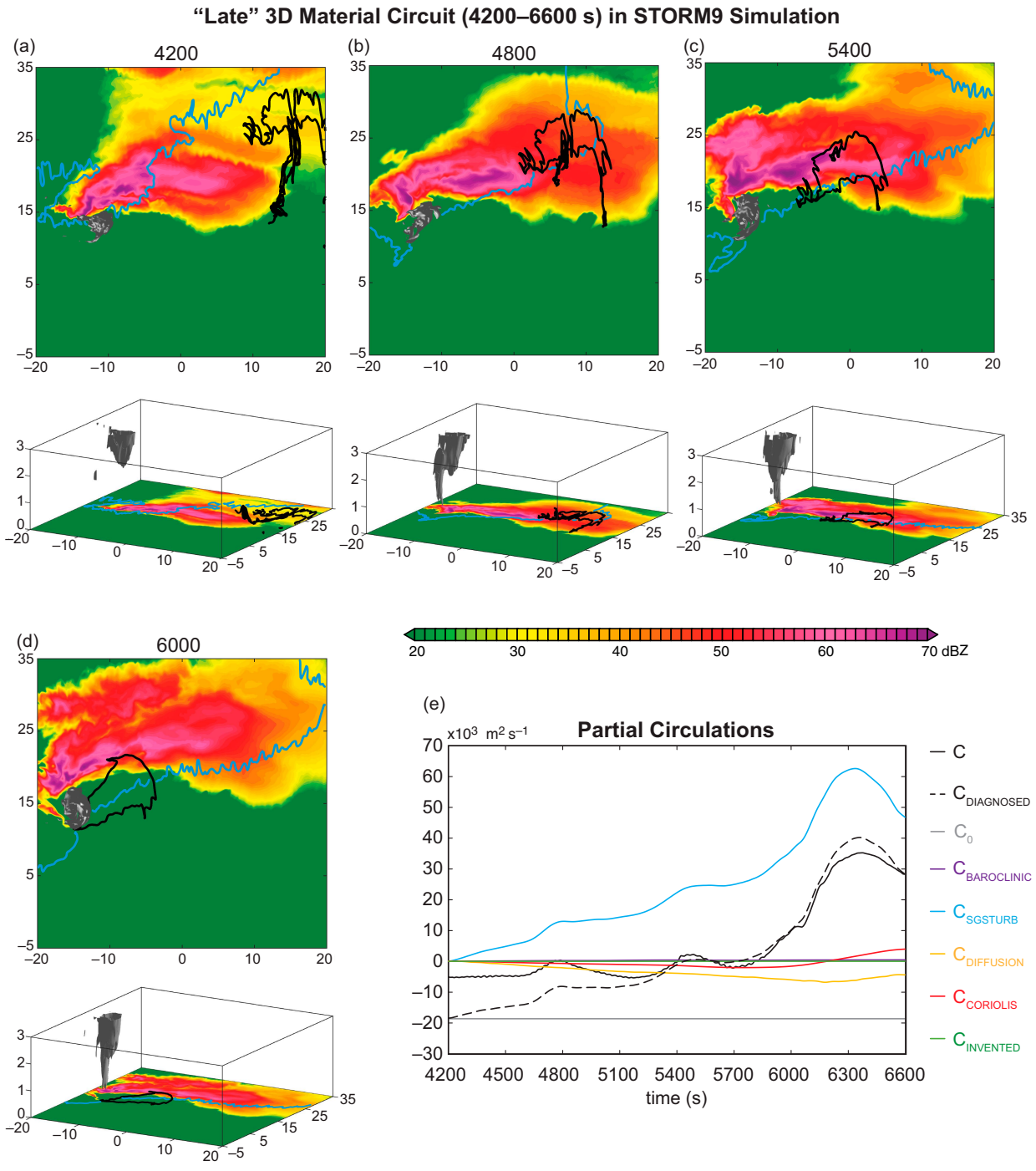

FIG. 17. As in Fig. 16, but for the material circuit that was tracked from 4200 to 6600 s in the STORM9 simulation.

at which point extrapolation of both velocities and the forcings in (4)–(7) is required, considerable extrapolation is nonetheless required in order to obtain the budget shown in Fig. 16e. For this reason, a second analysis was performed using a hybrid circuit, following the approach of Davies-Jones and Markowski (2021). Parcels within the hybrid circuit follow the three-dimensional velocity above $z = 15$ m (the first interior w grid level), but are not allowed to drop below this level. Instead, such parcels are constrained to follow the horizontal wind at $z = 15$ m and extrapolation is avoided. The analysis is included in the supplementary material. The key takeaway is that baroclinic generation of circulation is similarly absent.

TABLE 1. Summary of TLV characteristics. The time of axisymmetrization is the time at which a closed isobar exists at the lowest scalar level if contouring pressure every 1 mb. A TLV is defined as a vortex having $\zeta \geq 0.5\ s^{-1}$ on the lowest ζ grid and 10-m (ground-relative) wind speed exceeding 29 m s^{-1}.

Simulation	$\zeta \geq 0.05\ s^{-1}$ exceedance on scalar grid (s)	Axisymmetrization (s)	TLV period (s)	Peak 10-m wind (m s^{-1})/EF rating/time (s)
STORM9	5640	6000	6250–7230	62.7/EF3/6540
NOCOOL	5640	5730	5820–6360	49.5/EF2/5850
C20	6030	6090	6090–6690	83.2/EF4/6390

3) "LATE" MATERIAL CIRCUIT ANALYSIS: 4200–6600 S

A material circuit also is introduced at 6600 s (Fig. 17), during the time of the mature TLV, 60 s after its peak intensity (Table 1). The circuit's initial radius and altitude are the same as for the "early" circuit analyses. Perhaps not surprisingly, the circuit has a much larger circulation (~30 000 $m^2\ s^{-1}$) than the one introduced at 5940 s. The most notable findings, however, are the negative C_0 and the large positive contribution from $C_{SGSTURB}$ (Fig. 17e). These differences relative to the early circuit must ultimately be the result of different trajectories (per Fig. 11, there is a greater diversity of TLV parcel origins later). It is far from intuitive, but apparently this collection of parcels has a slight negative net barotropic vorticity (C_0), and also gains a lot of net positive circulation from the SGS turbulence scheme. The increased $C_{SGSTURB}$ is through the effects of surface drag, as opposed to SGS turbulent mixing in the model interior well away from the surface. During the time this circuit travels along the surface to the TLV region, significant storm-induced, near-surface, ground-relative wind accelerations occur along the path taken by the circuit. For example, a strong southerly wind acceleration occurs from 4200 to 6600 s immediately ahead of the updraft, and a strong northerly acceleration (decreasing southerlies) on the immediate cool side of the gust front (Fig. 18a). As explained in section 2d, owing to surface drag, accelerations of the near-surface ground-relative wind modify the near-surface horizontal vorticity ($\Delta\boldsymbol{\omega}_h$; Fig. 18b), and the circuit's C changes if $\Delta\boldsymbol{\omega}_h$ has a component normal to the surface defined by the circuit. The complexity of the circuit makes it

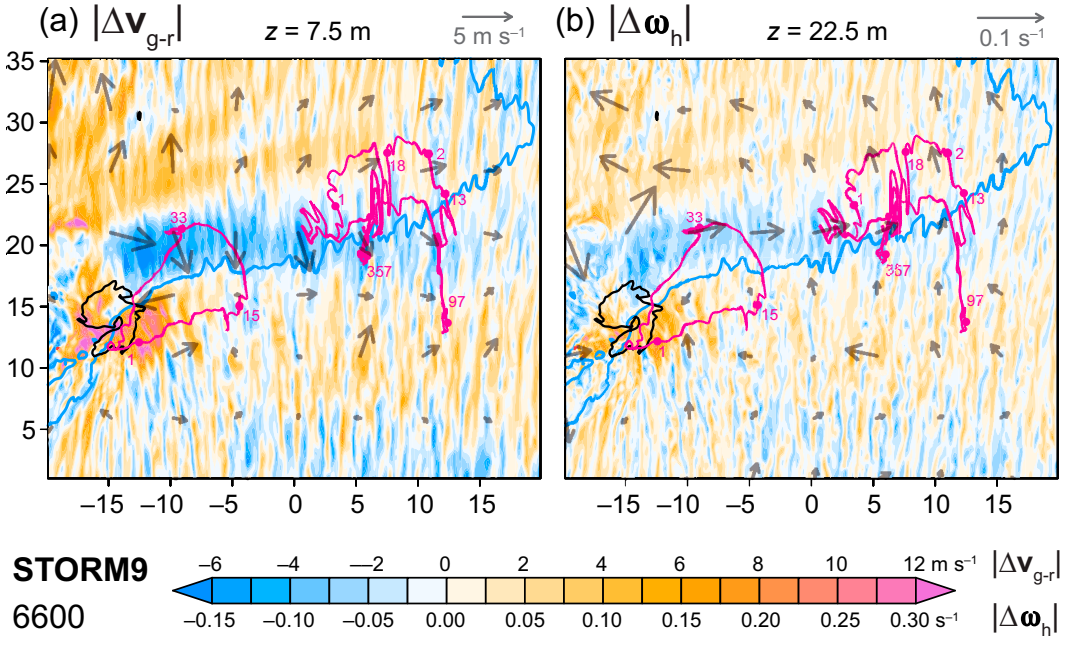

FIG. 18. (a) Horizontal cross section of the change in the ground-relative wind speed (shading) and the vector change in the ground-relative wind (vectors) at $z = 7.5$ m from 4200 to 6600 s. The $w = 6$ m s^{-1} isotach at $z = 993$ m (black contour) at 6600 s is overlaid, as is the $\theta'_\rho = -0.25$ K isopleth (light blue contour), which serves as a proxy for the gust-front location. The horizontal projections of the material circuit at 4800 and 6000 s also are overlaid (magenta curves; the westernmost is the circuit at 6000 s); altitudes of the curves (in m) are indicated at select points. Axis labels are in kilometers. (b) Horizontal cross section of the change in the horizontal vorticity magnitude (shading) and the vector change in the horizontal vorticity (vectors) at $z = 22.5$ m from 4200 to 6600 s. Vertical velocity, the gust front, and material circuits are overlaid as in (a).

virtually impossible to visualize such a 3D surface and how the flux of vortex lines through the surface would change in time. However, given the large growth of C_{SGSTURB} for this circuit, the associated changes in the horizontal vorticity ($\Delta\boldsymbol{\omega}_h$) apparently have a favorable component relative to the surface defined by the circuit. One additional noteworthy aspect of the $\Delta\boldsymbol{\omega}_h$ vectors is that they are opposite what we would expect if baroclinicity is dominating in the near-surface horizontal vorticity field in the forward-flank precipitation region, as it tends to in simulations with a free-slip lower boundary condition (e.g., Klemp and Rotunno 1983); the $\Delta\boldsymbol{\omega}_h$ vector pattern is counterclockwise in this region because of divergence in the ground-relative wind pattern and the influence of surface drag.

As was the case for the "early" circuit, circulation contributions from baroclinicity and the invented force are negligible (Fig. 17e). The contributions to C from numerical diffusion and the Coriolis acceleration are nonnegligible but still rather small, negative and positive, respectively (their magnitudes are ~15% of the magnitude of the total C).

3. Ancillary simulations

a. NOCOOL: A simulation without latent cooling

The evolution of the ζ field presented in section 2b (Fig. 5), specifically, how ζ anomalies within longitudinal surface-layer streaks amplify as they approach the gust front and overlying low-level updraft, with several TLV-genesis "near misses" preceding the eventual formation of an EF3 TLV, stimulates at least a couple of questions. What role, if any, does the gust front play in TLV formation? And is the gust front's interaction with the ζ streaks key? Based on a numerical simulation without latent cooling and a traditional gust front, hereafter referred to as the NOCOOL simulation, the answers to these two questions appear to be "unclear" and "no," respectively.

For the NOCOOL simulation, the National Severe Storms Laboratory (NSSL) double-moment microphysics scheme (Ziegler 1985; Mansell et al. 2010; Mansell and Ziegler 2013), which was used for all of the M20 simulations including the STORM9 simulation, is modified in the following ways: 1) evaporation is disabled; 2) melting and sublimation are allowed to occur, but their cooling of the air is disabled. Of course, in the NOCOOL simulation negative buoyancy is still present in the midst of hydrometeors; however, no outflow emanates from precipitation regions, and thus, there is no feature that really can be called a gust front.

A TLV develops in the NOCOOL simulation at 5820 s (Table 1; Fig. 19e), and it attains a maximum 10-m wind of 49.5 m s^{-1} (EF2) at 5850 s. The evolution of the ζ field in the NOCOOL simulation closely follows that of the STORM9 simulation (Figs. 19e,f), with positive-ζ anomalies amplifying as they pass beneath the overlying supercell updraft (see supplementary material for animations).

The low-level updrafts of the NOCOOL and STORM9 simulations have a similar structure and intensity, and though the reflectivity fields also are similar overall, the hook echo in the NOCOOL reflectivity field is less prominent in its southward extent (Figs. 19a,b). The most obvious difference in the θ'_ρ fields is that negative buoyancy is confined to precipitation regions in the NOCOOL simulation, though θ'_ρ is only ~−1 K in the heaviest precipitation. The low-level w field is more turbulent within the precipitation region of the NOCOOL simulation (the turbulent environment extends throughout the precipitation region) than in the STORM9 simulation, owing to the lack of latent cooling and turbulence-suppressing stabilization (Figs. 19c,d). The downdrafts in the precipitation region of the NOCOOL simulation also are weaker than in the STORM9 simulation [e.g., compare w near (−21, 21) in Fig. 19c with w near (−18, 16) in Fig. 19d].

b. C20: A twentieth century-style simulation

The elephant-in-the-room question is this: What happens in a simulation with the same environmental hodograph and sounding as the STORM9 environment, but with a laminar, horizontally homogeneous boundary layer and a free-slip lower boundary? A simulation with this "late-twentieth-century-style" configuration was also performed and hereafter is referred to as the C20 simulation. This was the industry standard approach to the numerical simulation of convective storms for decades, starting with the pioneering studies by Schlesinger (1975) and Klemp and Wilhelmson (1978). There is no invented force or Coriolis force in this simulation.

A TLV with peak 10-m winds of 83.2 m s^{-1} (EF4) develops in this simulation (6090–6690 s) (Table 1; Figs. 20–24). In contrast to the STORM9 simulation, the TLV in the C20 simulation develops on the *cool side* of the gust front, as in prior simulations in which the baroclinic mechanism (Davies-Jones 2000) has been implicated (e.g., Rotunno and Klemp 1985; Davies-Jones and Brooks 1993; Wicker and Wilhelmson 1995; Adlerman et al. 1999; Markowski and Richardson 2014b; Dahl et al. 2014; Parker and Dahl 2015; Dahl 2015) (Figs. 20e and 21e). Interestingly, the outflow is considerably stronger in the C20 simulation (minimum $\theta'_\rho \leq -6$ K at $z = 7.5$ m) than in the STORM9 simulation (cf. Figs. 20a,b and Figs. 21a,b), despite the use of identical microphysics parameterizations and virtually identical environments.[9] This is true not just based on the $z = 7.5$-m conditions, but also holds if a vertically averaged measure of cold pool strength is considered [e.g., the Rotunno et al. (1988) cold pool parameter; not shown]. The wall cloud in the C20 simulation (not shown) is roughly 100 m lower than in the STORM9 simulation as a result of the higher relative humidities associated with the cooler outflow, and the ζ maximum is centered within it, in contrast to the STORM9 simulation.

The horizontal vorticity fields in the C20 and STORM9 simulations differ considerably (Figs. 20c,d and 21c,d). Horizontal vorticity is greatly enhanced, relative to the environment, on the western side of an internal boundary within the forward-flank precipitation that Beck and Weiss (2013) termed a *left-flank*

[9] One unavoidable (and probably minor) issue with the C20 simulation is that the base-state, near-surface Richardson number is <0.25; thus, SGS turbulent kinetic energy is generated, which results in SGS mixing that slightly reduces the vertical shear in the lowest few hundred meters over the course of the 2-h simulation (≈2 m s^{-1} reduction in the magnitude of the vector wind difference over the lowest 250 m).

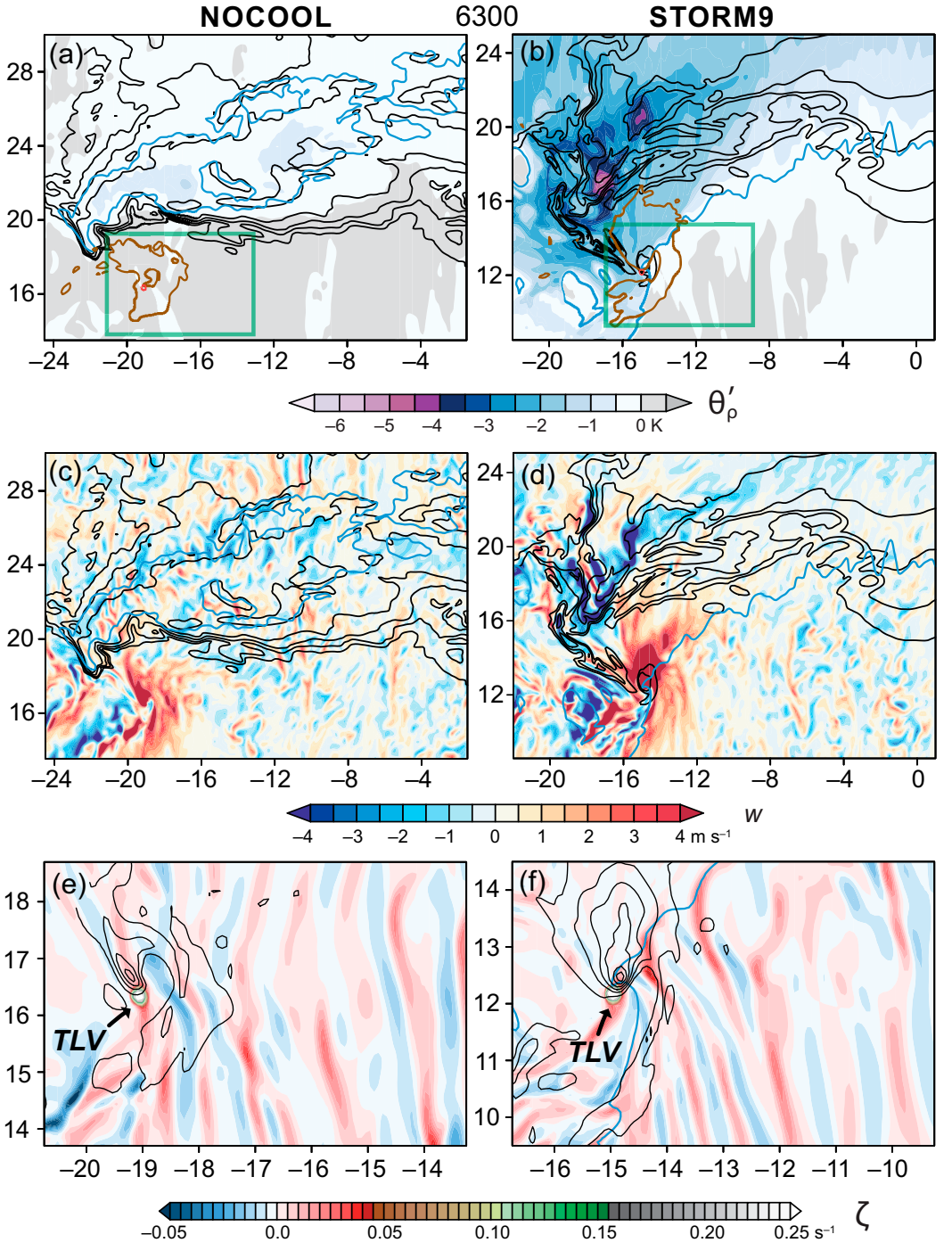

FIG. 19. Comparison of select fields in the (a),(c),(e) NOCOOL and (b),(d),(f) STORM9 simulations at 6300 s. (a),(b) Horizontal cross sections of θ'_ρ at z =7.5 m (color shading), the w = 6 m s^{-1} isotach at z = 993 m (brown contours), the ζ = 0.10 s^{-1} isovort at z = 7.5 m (red contours), and reflectivity at z = 522 m (black contours of 20, 30, 40, 50, and 60 dBZ). The θ'_ρ = −0.25-K isopleth (bold blue contour) is also overlaid. The magenta box encloses the zoomed-in regions shown in (e) and (f). (c),(d) Horizontal cross sections of w at z = 266 m (color shading). Reflectivity and the θ'_ρ = −0.25-K isopleth are overlaid as in (a) and (b). (e),(f) Close-up depiction of horizontal cross sections of ζ at z =7.5 m (color shading) and w at z = 522 m (black isotachs of 5, 10, 15, 20, 25 m s^{-1}). In (f), the θ'_ρ = –0.25-K isopleth is also overlaid. Axis labels are in kilometers in all six panels.

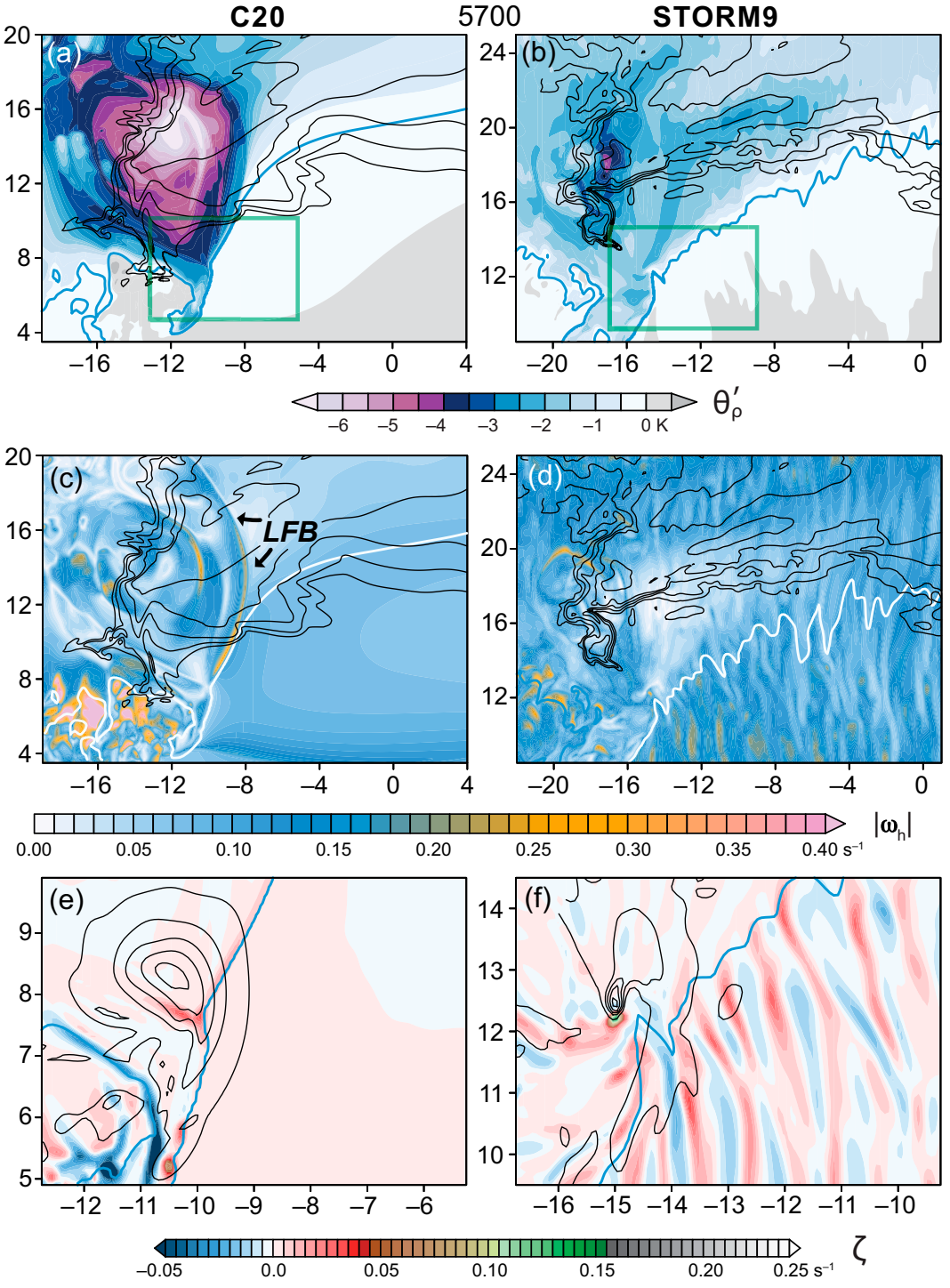

FIG. 20. Comparison of select fields in the (a),(c),(e) C20 and (b),(d),(f) STORM9 simulations at 5700 s. (a),(b) Horizontal cross sections of θ'_ρ at z = 7.5 m (color shading) and reflectivity at z = 522 m (black contours of 20, 30, 40, 50, and 60 dBZ). The magenta box encloses the zoomed-in regions shown in (e) and (f). (c),(d) Horizontal cross sections of horizontal vorticity magnitude at z = 22.5 m (color shading) and reflectivity at z = 522 m [same contour levels as in (a) and (b)]. In (c), "LFB" refers to the Beck and Weiss (2013) left-flank boundary. (e),(f) Close-up depiction of horizontal cross sections of ζ at z =7.5 m (color shading) and w at z = 522 m (black isotachs of 5, 10, 15, 20, 25, … m s^{-1}). In all six panels, axis labels are in kilometers and the θ'_ρ = −0.25-K isopleth [bold blue contour in (a), (b), (e), and (f); bold white contour in (c) and (d)] is overlaid and serves as a gust-front proxy.

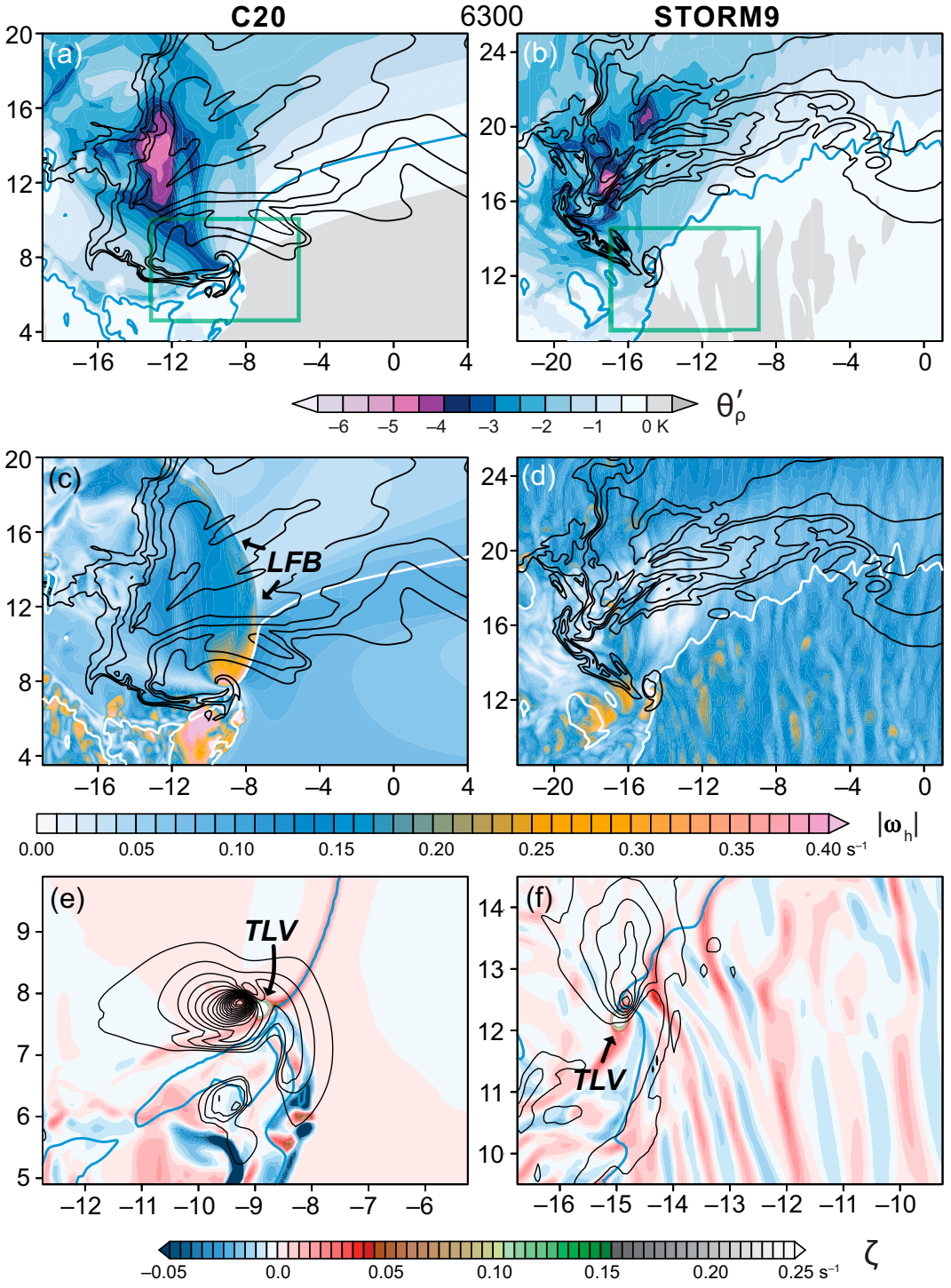

FIG. 21. As in Fig. 20, but for 6300 s.

boundary (Figs. 20c and 21c). The enhancement is largely the result of baroclinic horizontal vorticity generation (e.g., Klemp and Rotunno 1983). No left-flank boundary is obvious in the STORM9 simulation (Figs. 20d and 21d), and in fact horizontal vorticity is a relative *minimum* in the STORM9 simulation in the outflow north of the updraft, owing to the reduced ground-relative winds in this region and the use of the semislip lower boundary condition.

The trajectories feeding the incipient TLV as the ζ maximum undergoes axisymmetrization originate exclusively in the outflow

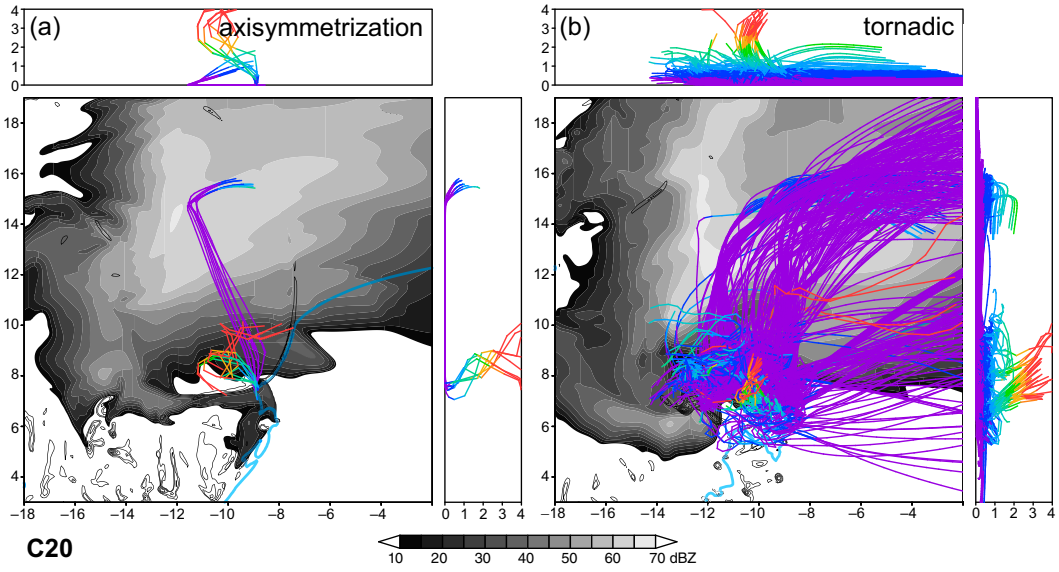

FIG. 22. Trajectories of parcels in the C20 simulation that attain $\zeta \geq 0.05\ s^{-1}$ below $z = 22.5$ m (the second grid level for ζ) during the (a) axisymmetrization period (6030–6090 s) and (b) tornadic period (6090–6960 s). Trajectories are plotted from 5400 s (the time that parcels are introduced into CM1) until 6270 and 6900 s in the respective panels; gust fronts, reflectivity (gray shading), and vertical vorticity at $z = 7.5$ m (0.01, 0.02, 0.04, 0.06, …, 0.40 s^{-1}) are also displayed in each panel at these times. Parcels that dip below $z = 7.5$ m at any point in their journey are excluded. The colors of the trajectories vary with altitude.

(Fig. 22a), i.e., on the cool side of the gust front, also in contrast to the STORM9 simulation but consistent with prior numerical simulation studies (e.g., Rotunno and Klemp 1985; Davies-Jones and Brooks 1993; Wicker and Wilhelmson 1995; Markowski and Richardson 2014b; Dahl et al. 2014; Boyer and Dahl 2020; Fischer and Dahl 2022). As in Fischer and Dahl (2022), once a TLV is established, trajectories feeding the TLV originate in both the outflow and in the environment (Fig. 22b). (The vortex is on the cool side of the gust front, but parcels diffuse through the gust front via SGS mixing and/or numerical diffusion.) Moreover, analyses of the development of circulation about both a 3D material circuit (Fig. 23) and a hybrid circuit (supplementary material) implicate baroclinic generation as the primary circulation source, as found in all prior known numerical simulation studies using the C20 methodology (e.g., Rotunno and Klemp 1985; Davies-Jones and Brooks 1993; Wicker and Wilhelmson 1995; Adlerman et al. 1999; Dahl et al. 2014).

Regarding the vortex lines (Fig. 24), those that enter the low-level mesocyclone all originate in the forward-flank outflow northeast of the updraft (cf. Fig. 15). Some vortex lines rise through midlevels, and others subsequently descend into the rear-flank outflow. The latter form arches like those documented by Rotunno and Klemp (1985), Straka et al. (2007), Markowski and Richardson (2014b), Markowski et al. (2008, 2011, 2012a, 2014), Marquis et al. (2012), and Kosiba et al. (2013).

4. Discussion

The analyses of sections 2 and 3 reveal several key differences in how the TLV develops in the STORM9 simulation compared with the consensus understanding built on many decades of numerical simulations and field observations. Though nothing about the evolution of the larger-scale aspects of the STORM9 simulation looks unusual (e.g., the storm's reflectivity, updraft, downdraft, and outflow structure, or the location of TLV development; Fig. 3), a close inspection of (i) the details of the evolution of the ζ field, (ii) trajectories, (iii) Lagrangian analyses of the sources of circulation, and (iv) vortex lines tells a different tale. Specifically, with respect to (i), the initial ζ amplification occurs within longitudinal ζ streaks in the environmental air mass, rather than within the outflow or along the gust front. With respect to (ii), the incipient TLV is fed exclusively by environmental air parcels until axisymmetrization occurs. With respect to (iii), the TLV's primary circulation source is vorticity in the environment, or environmental vorticity modified by surface drag, as opposed to baroclinically generated circulation. Not surprisingly, the vortex lines referenced in (iv) that are constructed through the TLV also originate in the environment.

It would seem that at least one of the following must be true:

1) prior supercell simulations that have used laminar, horizontally homogeneous environmental boundary layers develop TLVs (if their resolution permits), and perhaps also near-surface mesocyclones, for the wrong reasons;
2) the M20 supercell simulations develop TLVs for the wrong reasons;
3) supercell tornadoes form in a wide range of ways in the real atmosphere, even within supercells that appear to be similar, and increasingly realistic numerical simulations are finally now capturing that diversity (if true, additional environmental ingredients might be worthy of consideration in tornado forecasting).

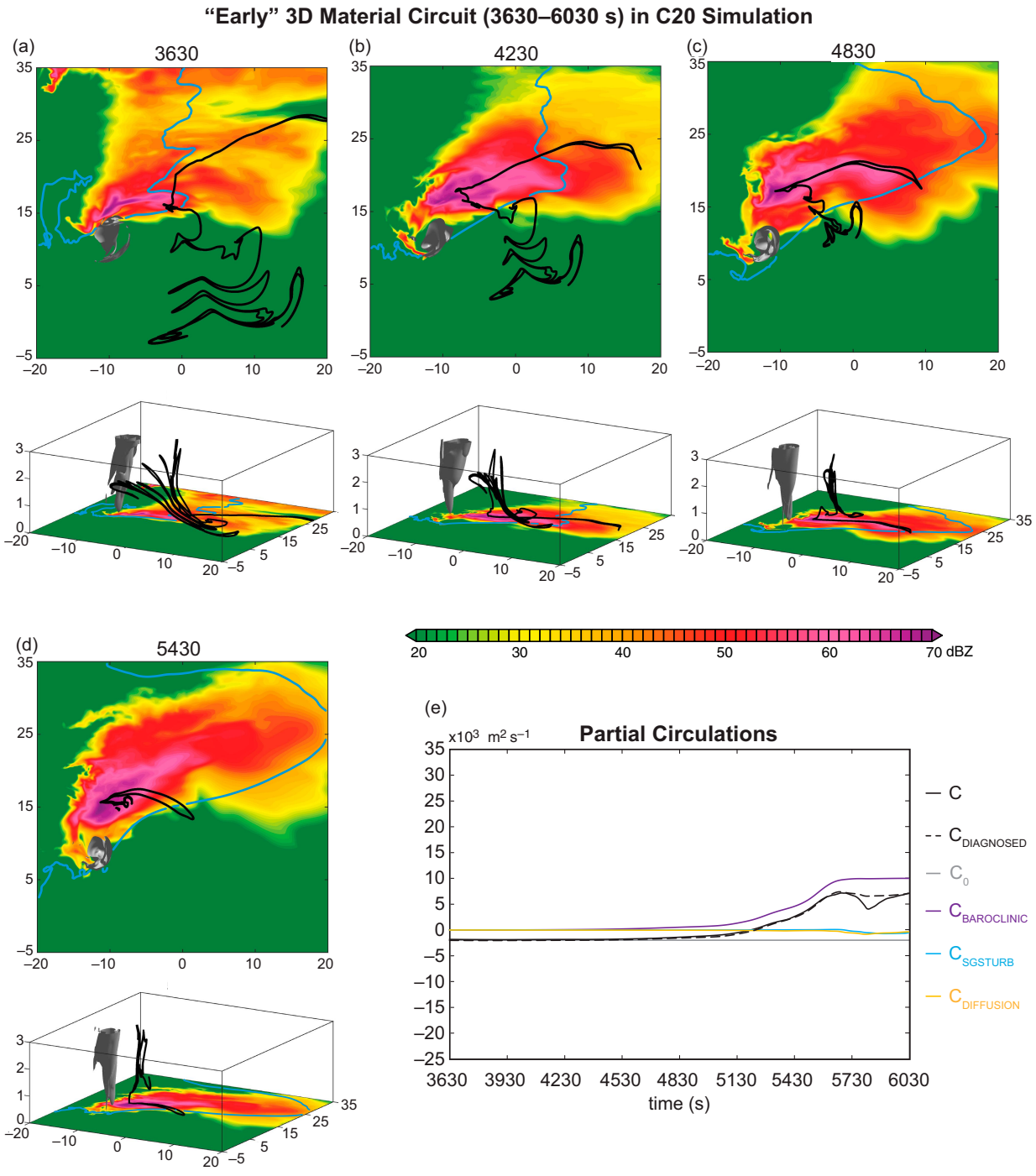

FIG. 23. As in Fig. 16, but for the material circuit that was tracked from 3630 to 6030 s in the C20 simulation.

How can the findings presented herein be squared with past studies? As explained in section 1, M20 is one of the only numerical modeling studies of supercell storms in which turbulent eddies are present in the environment. The Nowotarski et al. (2015) simulations also included an environmental boundary layer with resolved turbulence, but the resolution was somewhat marginal (Δx = 200 m, Δz = 50 m) and the simulations lacked TLVs anyway. Virtually all other prior simulation studies have laminar boundary layers in the environment, even in the Orf et al. (2017) simulation (Δx = 15 m).

In the pioneering simulation studies of the 1980s and 1990s (e.g., Rotunno and Klemp 1985; Davies-Jones and Brooks

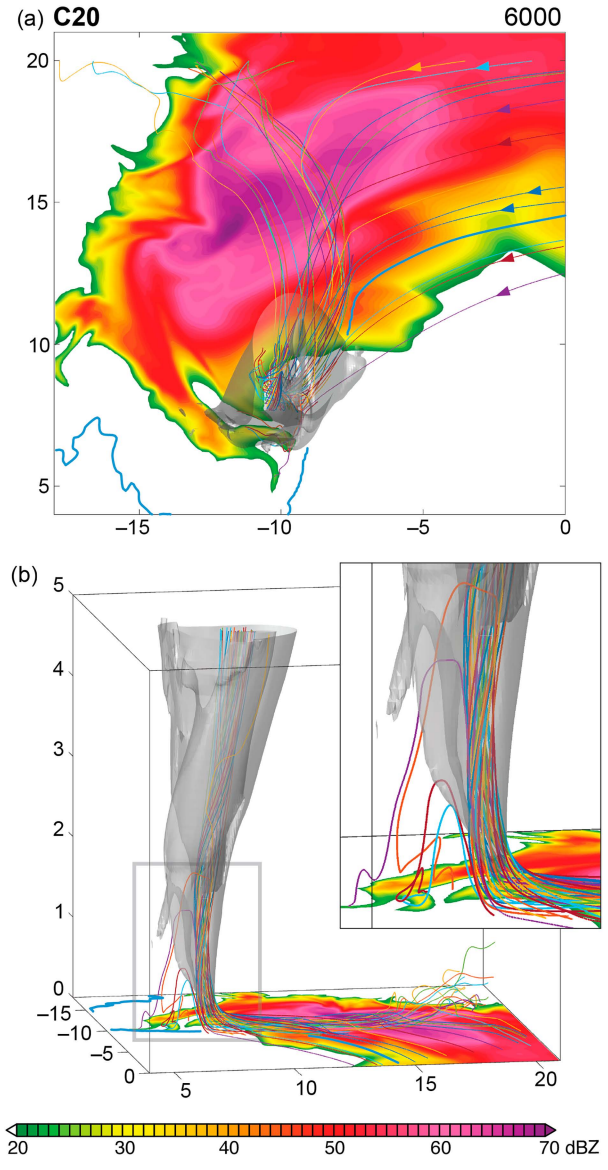

FIG. 24. Vortex lines in the C20 simulation at 5940 s, viewed from (a) above and (b) from the east-southeast. Each vortex line has a different color. The vortex lines all pass through grid points at which $\zeta \geq 0.05\ s^{-1}$ at $z = 266$ m. The $w = 20\ m\ s^{-1}$ isosurface (gray), reflectivity at $z = 7.5$ m (color shading), and gust front (thick blue contour) also are displayed. Axis labels are in kilometers. Vortex lines are terminated where they pass below $z = 15$ m (the lowest grid level where centered-difference estimates of the horizontal vorticity are available).

1993; Wicker and Wilhelmson 1995, among others), the cold pools are probably too strong (Markowski 2002) and the environment is laminar. In a laminar environment, there is of course no possibility of surface-layer ζ streaks from the environment playing a role in TLV genesis. Perhaps the baroclinic mechanism, in which parcels acquire significant ζ next to the surface after passing through a downdraft and accompanying horizontal buoyancy gradients, is merely the only way a near-surface mesocyclone or TLV can form in these simulations. The NOCOOL simulation confirms that outflow and downdrafts driven by latent cooling are not essential for TLV formation. As explained in section 1a, Davies-Jones (1982a,b; Davies-Jones et al. 2001) argued that a downdraft is necessary for the development of near-surface ζ in the absence of preexisting near-surface ζ. Though he had storm-scale downdrafts driven by negative buoyancy in mind, perhaps the ubiquitous downdrafts in a turbulent boundary layer are all that is needed.

Cold pool differences between the STORM9 and C20 simulations aside, why would the baroclinic mechanism operating in the C20 simulation completely vanish in the STORM9 simulation simply because the environment is turbulent? One speculation is that, as long as sufficiently strong, near-surface, dynamically driven (near-surface buoyancy is typically zero or negative in the TLV formation region) upward accelerations are present (such accelerations would most often require a supercell updraft in strong low-level shear), TLV formation merely happens where the most "accessible" near-surface ζ is found. Though there is near-surface ζ in the outflow in the STORM9 simulation, the environmental air has even larger near-surface ζ, so this is where ζ amplification is facilitated. In the C20 simulation, the only near-surface ζ is confined to the cool air, and so TLV genesis is initiated in the cool air. The near-surface horizontal vorticity also is larger in the environment than in the forward-flank outflow in the STORM9 simulation; the opposite is the case in the C20 simulation.

Of course, the findings herein must also be compared with past observational studies, not merely past numerical modeling studies. Observational studies, specifically, dual-Doppler wind syntheses, also have found that the trajectories enter the tornadic region of supercells after first descending through extensive precipitation and downdraft (e.g., Brandes 1978, 1984; Wakimoto et al. 1998; Ziegler et al. 2001; Markowski et al. 2012a,b; Kosiba et al. 2013). Can the trajectories of the STORM9 simulation be squared with these robust prior findings? In the observational studies, however, the analyses are almost always more than two hours after convection initiation (the M20 simulations were only run out to $t = 2$ h), and usually after a tornado is already in progress. Moreover, the dual-Doppler wind syntheses rarely extend far into the environment, owing to insufficient clear-air scatterers and/or radar sensitivity. In the STORM9 simulation, once the TLV is established, trajectories pass through the cold pool and downdrafts, as in prior observational studies.

The STORM9 simulation's TLV initially ingesting environmental air and then later, following axisymmetrization, ingesting outflow air, is opposite the evolution envisioned by Fischer and Dahl (2022). In their simulation, which was configured like the C20 simulation in section 3b, the initial near-surface ζ development occurs in the cold air, and only after vorticity axisymmetrization does air from all quadrants feed the vortex. One might also wonder how a wall cloud is present in STORM9 prior to TLV genesis if environmental air feeds the incipient TLV (Fig. 10). As explained in section 2d, the parcels feeding the wall cloud in the STORM9 simulation indeed originate in the cool, humidified outflow, but the developing ζ maximum at cloud base was displaced slightly away from the cloud-base

lowering (Fig. 10b). If this subtlety were to exist in a real storm, it might be difficult to observe without extremely careful stereophotogrammetric observations (Atkins et al. 2014). The author's sense is that supercell cloud bases frequently have chaotic motions that can make it difficult to pin down the precise position of a ζ maximum within the cloud base until a funnel has formed.

The vortex lines analyzed within and near low-level mesocyclones observed in prior dual-Doppler wind syntheses might be the most difficult to reconcile with the present study. These studies (e.g., Straka et al. 2007; Markowski et al. 2008, and other references cited in section 3b) have repeatedly found the vortex lines passing through the low-level mesocyclone region to have horizontal projections lying on the cool side of the gust front, aligned with the isentropes and/or gust front (in some cases only the gust-front position was known). These observations were interpreted as being an indication that the vortex lines were heavily influenced by baroclinic horizontal vorticity generation, and this notion was consistent with the numerical modeling studies of Rotunno and Klemp (1985), Davies-Jones and Brooks (1993), and Adlerman et al. (1999), among others, which implicated the baroclinic mechanism of near-surface ζ development. Although the vortex lines in the C20 simulation are similar to those in the aforementioned studies, the vortex lines that pass through STORM9's mesocyclone region in the lowest few hundred meters are environmental vortex lines at all stages of the storm's evolution. Perhaps STORM9 has key dynamical differences relative to prior observed storms, or perhaps the smoothing of vortex lines in prior studies, in addition to a general inability to observe vortex lines in the environment and very near to the surface (owing to vertical radar beam spacing and smoothing inherent in the dual-Doppler wind synthesis), has provided a misleading picture.

One other past observational study difficult to reconcile with the STORM9 simulation is that of Markowski et al. (2012b), specifically, their material circuit analyses. Their analyses diagnosed large gains in circulation by the circuits as they crossed the forward-flank baroclinic zone of the 5 June 2009 tornadic supercell intercepted by the Second Verification of the Origins of Rotation in Tornadoes Experiment (VORTEX2; Wurman et al. 2012). The circuits lacked significant circulation in the far field, implying that environmental vorticity was not a significant circulation source for the low-level mesocyclone. However, some liberties were taken in assuming a steady-state wind field in order to extend the trajectories backward in time to a position far upstream of the incipient tornado. Moreover, the circuits were much wider and introduced at a higher altitude than the circuits used in the STORM9 analysis in section 2e. Thus, the comparison of the STORM9 and Markowski et al. (2012b) material circuit analyses is unlikely to be an "apples-to-apples" comparison.

Even though the use of a turbulent environment in the STORM9 simulation might tempt one to conclude that the simulation is superior to others in terms of its realism, there is plenty to be skeptical of. The difference in cold pool strength between the STORM9 and C20 simulations (the latter is considerably colder, and is associated with stronger baroclinicity as a result) is particularly disturbing. Microphysics parameterizations are tuned using simulations run more like the C20 simulation, and typically at coarser resolutions. The parameterization of near-surface turbulence (including the lower boundary condition) is also problematic, as has been discussed in several recent articles (Markowski 2016; Markowski and Bryan 2016; Wang et al. 2020, 2023). Getting the near-surface turbulence "right" is critical if we are to have any hope of assessing the credibility of the processes documented in the STORM9 simulation. The STORM9 simulation also lacks radiative transfer processes and surface heat fluxes. What if cloud shading (Markowski et al. 1998; Frame and Markowski 2010, 2013) suppresses the environmental turbulence (Nowotarski and Markowski 2016)? How might ground wetted and cooled by rain influence the evolution?

This study spawns at least as many questions as it answers. Among the most interesting, from the author's perspective, are the following:

- *Do the longitudinal positive-ζ streaks in the surface layer* facilitate *TLV formation (i.e., would TLVs fail to form in their absence?), or are the positive-ζ streaks merely sites for TLV formation?* The fact that ζ amplification in the C20 simulation is confined to the cool side of the gust front and is not the result of the tilting of environmental vortex lines might seem to imply that the environmental vortex-line corrugations in the STORM9 simulation are indeed facilitators of TLV formation. It is tempting to wonder if a suitable analogy is that the vortex-line corrugations act a bit like snags in a sweater that can be tugged on. The vorticity tilting and stretching experienced by the environmental parcel bound for the incipient TLV in the STORM9 simulation, just 15 m above the surface (approaching 10^{-2} s^{-2}; Fig. 13f), would seem difficult to attain in a laminar, horizontally homogeneous environment. It would be difficult to test this question with a semislip lower boundary condition, because without the resolved coherent turbulent structures in the boundary layer, a semislip boundary would result in large, unrealistic accelerations in the simulation's environment (Markowski and Bryan 2016).
- *What is "special" about supercell storms?* One common previously held assumption is that supercells are uniquely suited for tornadogenesis because they are the only storms that can feed on their own outflow, and significant ζ and circulation are limited to the outflow air mass. Perhaps supercells are special simply because of their large near-surface $\partial w/\partial z$. Yet to be addressed would be why all supercells do not spawn tornadoes. Perhaps this could be due to variations in near-surface $\partial w/\partial z$ from storm to storm, and/or the organization of surface-layer turbulence.
- *Does it matter that the positive-ζ anomalies in the surface layer are stronger than the negative-ζ anomalies?* If so, this would imply another indirect role of the Coriolis force (in conjunction with drag in the boundary layer, another indirect role of the Coriolis force is to promote the curved hodographs that favor cyclonically rotating, right-moving supercells, e.g., Fig. 1b). "Indirect" here refers to a way other than the generation of circulation. Or is the mere presence of

corrugations in the vortex lines all that matters, because once vortex lines are tugged upward by an overlying updraft, the corrugations vanish anyway (Fig. 13), and positive ζ inevitably ends up in updraft given that the environmental vortex lines are highly streamwise with respect to the storm-relative flow? [An additional ancillary simulation without a Coriolis acceleration (NOCOR) was performed at the request of a reviewer and is included in the supplementary material. Unfortunately, the removal of the Coriolis acceleration results in a different environment, one that is characterized by less hodograph curvature, weaker vertical wind shear, less SRH, and ultimately a storm with a much weaker low-level updraft. No TLV develops, but the failure of an intense vortex to form is likely attributable to the weaker low-level updraft rather than lack of a Coriolis acceleration.]

5. Summary and conclusions

This article investigated the formation of a strong TLV in one of the numerical simulations that was part of a prior study on the intrinsic predictability of tornadic supercells. The kinematics and dynamics of TLV formation were found to be rather different from the community's current understanding stemming from roughly a half century of simulations and observations. Though the evolution of the larger-scale aspects of the tornadic storm (e.g., its reflectivity, updraft, downdraft, and outflow structure, the location of TLV development) was unremarkable, an analysis of the small-scale details within the rapidly evolving ζ field, and associated vortex lines and trajectories, including Lagrangian analyses of the sources of circulation, revealed key differences between TLV genesis herein and widely held conceptual models.

The key difference between the simulation in this study and those in prior simulation studies was the inclusion of a turbulent environmental boundary layer. Prior simulation studies have almost exclusively used a laminar environmental boundary layer, either because of resolution limits or the lack of a mechanism for triggering turbulence. Prior observational studies, at least those that rely on radar data, typically have not been suited for detecting the sorts of processes identified in this article as being key to TLV formation.

The key aspects of TLV genesis found in this investigation are summarized schematically in Fig. 25. Coherent turbulent structures in the surface layer are aligned with the approximately southerly ground-relative winds. The eddies resemble the legs of hairpin vortices that have been extensively studied in the boundary layer and turbulence communities. The eddies are responsible for longitudinal (approximately north–south-oriented) ζ streaks via the tilting of the mean environmental horizontal vorticity. In other words, the approximately north–south-oriented eddies corrugate (in the vertical plane) the west–east-oriented environmental vortex lines. Within the positive-ζ streaks, ζ exceeding 0.03 s^{-1} is present as low as $z = 7.5$ m.

The overlying storm updraft draws environmental vortex lines upward. The environmental vorticity in the surface layer is almost purely streamwise in the storm's reference frame, given the storm motion toward the northeast, the ground-relative winds from the south, and the mean vorticity pointing to the west. Thus, the updraft-scale tilting of the vortex lines results in positive ζ being collocated with strong upward accelerations. Even parcels having negative ζ in the surface layer rapidly acquire positive ζ as they ascend owing to the updraft-scale tilting of the streamwise horizontal vorticity. However, the large, "preexisting," near-surface ζ in the environment ahead of the storm is key: the positive near-surface ζ perturbations associated with the longitudinal streaks serve as seeds for TLV formation as they are overrun by the supercell updraft. Accelerations of the ground-relative winds ahead of the storm associated with the intensification of the TLV generate additional horizontal vorticity in the storm's inflow owing to surface drag, and this becomes an additional source of circulation for the mature TLV. Trajectories into the developing TLV are initially from the environmental side of the gust front, but later feed the vortex from both the cool and warm sides of the gust front, though at no point in the life cycle of the TLV is baroclinic vorticity generation a significant source of circulation for the TLV.

Even though only one member of the M20 ensemble was analyzed in this article, the other M20 simulations exhibit similar behaviors. The good news is that the relevance of environmental parameters heavily relied upon for discriminating between tornadic and nontornadic supercells—for example, low LCLs and strong low-level shear (e.g., Thompson et al. 2003)—remains unchanged even if surface-layer processes in the turbulent environment are important. High LCLs, which tend to be associated with strong cold pools, would seem to be detrimental to the chain of processes documented herein. Such excessive outflow would seem likely be disruptive to the reorientation and amplification of vorticity originating in the environmental surface layer if the main updraft is repeatedly undercut by outflow. A lack of strong low-level shear would imply a weak upward-directed dynamic vertical pressure-gradient force, which would also seem to be unfavorable for the uplifting of near-surface environmental vortex lines.

If the ζ streaks actually facilitate TLV formation in real storms, the implications are potentially enormous, as tornado forecasting should then also consider whether environmental conditions might favor hairpin vortices or any other coherent turbulent structures. For example, surface wind speed and surface heat flux would likely be relevant. Curiously, in a prior study (Markowski et al. 2003), ground-relative winds were found to be as good a discriminator between tornadic and nontornadic supercells as more popular forecasting parameters, with faster winds being more favorable for tornadoes. Moreover, storm chasers frequently eagerly await the early evening transition (sometimes termed "6 o'clock magic"), which marks the end of the time of day with a strong positive surface heat flux. Surface-layer streaks are most likely to be observed in windy conditions without a strong surface heat flux.

Regardless of the answer to the provocative statement toward the beginning of section 4 ("it would seem that at least one of the following must be true"), the findings of this article, at the very least, illustrate the need for (i) continued efforts to improve microphysical parameterizations used in numerical models, or at least explore their performance in simulations in

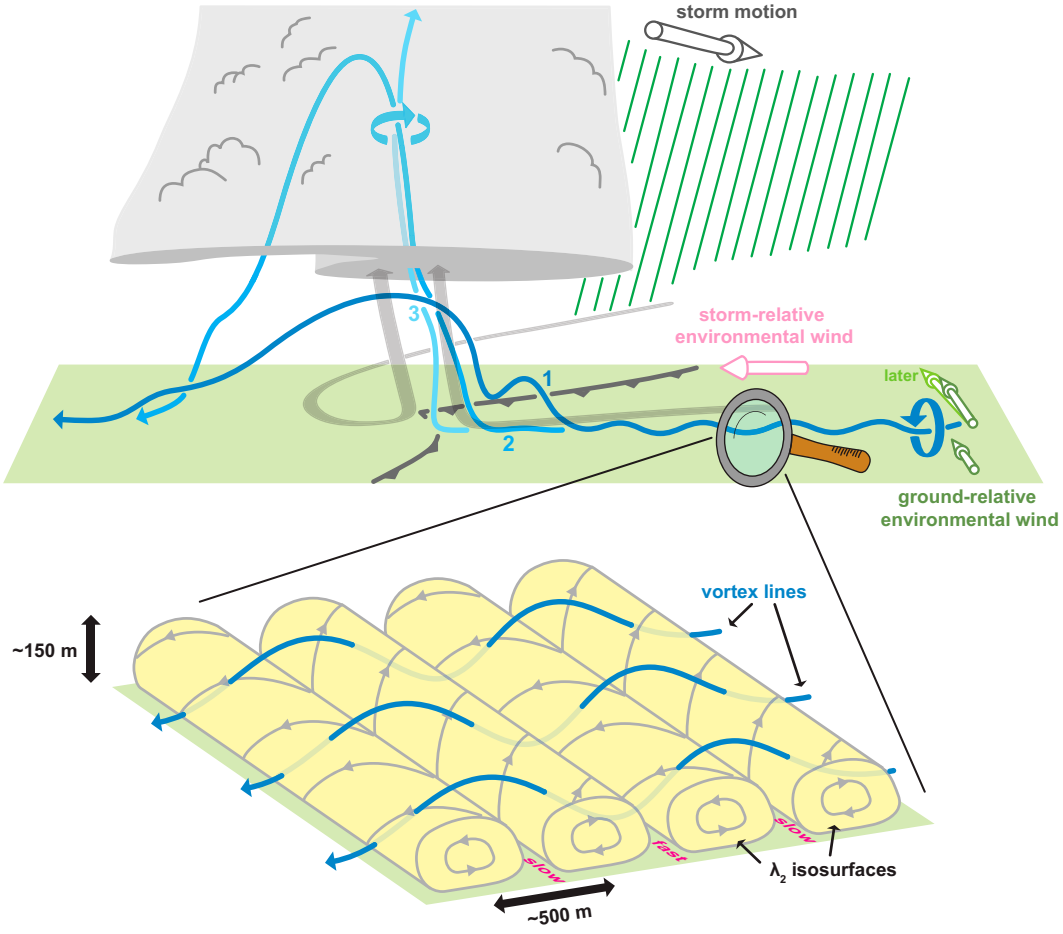

FIG. 25. Schematic summarizing the key aspects of the STORM9 simulation associated with tornadogenesis. The vortex lines (shades of blue) labeled "1," "2," and "3" can represent either a single vortex line at multiple times through a parcel approaching the developing TLV, a la Fig. 13, or different vortex lines at a single time drawn through locations increasing upstream of the developing TLV. The broad gray arrows indicate (storm-relative) trajectories feeding the TLV from the environment and from the precipitation and outflow (precipitation/outflow trajectories enter the developing TLV only once the flow associated with the intensifying ζ maximum becomes highly "axisymmetrized"). In the close-up of the environmental surface layer (bottom of figure), the gray streamlines indicate ground-relative perturbation winds associated with surface-layer eddies. The locations of alternating surface streaks of fast and slow wind speed are also indicated.

which a large fraction of the turbulence is resolved, (ii) continued efforts to improve the handling of near-surface turbulence (including the lower boundary condition), which is always going to be underresolved near the surface, regardless of the model resolution, (iii) the inclusion of additional processes (e.g., radiative transfer, surface heat and moisture fluxes, ground fluxes) that are routinely presumed to be of secondary importance but might alter conceptual models in unexpected ways, and (iv) continued pursuit of methods for obtaining volumetric buoyancy observations in supercell storms (e.g., Riganti and Houston 2017; Bartos et al. 2022), especially given the cold pool differences between the STORM9 and C20 simulations.

Acknowledgments. The author is grateful for discussions pertaining to this work with Johannes Dahl, Ying Pan, Matt Parker, Yvette Richardson, Rich Rotunno, Lou Wicker, and George Young, and for the development and long-standing support of CM1 by George Bryan. The author also thanks Rich Rotunno, Lou Wicker, and an anonymous reviewer for their careful reading of this lengthy article and comprehensive reviews, and Matt Bunkers for his comments on an earlier version of the article. A large fraction of the figures was created using MATLAB and the Grid Analysis and Display System (GrADS). GrADS was developed by the Center for Ocean–Land–Atmosphere Studies. Figure 1 was created using GrADS software written by Bob Hart. Aaron Wang provided MATLAB code for computing λ_2. Vis5d was also heavily used for visualization in the course of this work, though not for final figure production. The numerical simulations were performed on the Roar supercomputer at Penn State's

Institute for Computational and Data Sciences (ICDS). This research was funded by National Science Foundation Award AGS-2150792.

Data availability statement. All simulation output created during this study, along with the analysis software, is openly available from the Penn State DataCommons at https://doi.org/10.26208/6DSC-TS33.

APPENDIX A

Numerical Model Configuration

The M20 numerical simulations were performed using CM1, release 18.3 (Bryan and Fritsch 2002). As explained in section 1, 25 supercell simulations were performed in environments in which turbulent eddies are explicitly resolved (turbulence is triggered via random temperature perturbations of up to ±0.25 K in the initial conditions), and the environments have identical horizontal mean fields and are extremely favorable for tornadoes [the environment is characterized by surface-based CAPE of 3683 J kg^{-1}, 0–1-km (0–3-km) storm-relative helicity of 227 (300) m^2 s^{-2}, and a significant tornado parameter of 6.1; Fig. 1]. The 25-member ensemble was generated by using 5 different boundary layer realizations (5 different random number seeds were used) and 5 different warm-bubble-insertion locations; a warm bubble is inserted into each simulation after a 12-h spinup period in order to initiate deep moist convection.

The domain is 127.5 km × 127.5 km × 18.0 km (1700 × 1700 × 121 grid points), the horizontal grid spacing is everywhere 75 m, and the vertical grid spacing varies from 15 m at the surface to 285 m at the top of the domain. The lateral boundaries are periodic, and the top boundary is rigid and free slip. At the lower boundary, the semislip boundary condition is used, with the roughness length set to 12 cm (this corresponds to a nondimensional drag coefficient of 0.0094). An adaptive large and small time step was used, and throughout most of the simulations, these are approximately 1.0 and 0.125 s, respectively. Subgrid-scale turbulence is parameterized using a turbulent kinetic energy scheme (Deardorff 1980). The cloud and precipitation microphysics is parameterized using the NSSL double-moment scheme (Ziegler 1985; Mansell et al. 2010; Mansell and Ziegler 2013). The Coriolis acceleration is included (f plane assumed, with $f_0 = 10^{-4}$ s^{-1}), but it only acts on horizontal velocity perturbations relative to the initial, base state (the implications are addressed in appendix B). Surface heat and moisture fluxes are excluded, as are radiative transfer processes. Additional details can be found in M20's Table 1.

APPENDIX B

Comments on the "Invented" Force in the M20 Simulations

As a result of the Coriolis acceleration only being applied to horizontal velocity departures from the initial, base state (Fig. 1b, blue hodograph), the M20 simulations contain an "invented" force that Davies-Jones (2021) has cautioned about. Given that this article claims to have identified a possible new tornadogenesis mechanism, it is worth ensuring that the results of this study have not been adversely influenced by such an artifact.

Horizontal accelerations in the real atmosphere are governed, to a good approximation (i.e., by approximating the Coriolis acceleration as $f_0\mathbf{k} \times \mathbf{v}_h$), by

$$\frac{d\mathbf{v}_h}{dt} = -\alpha\nabla_h p - f_0\mathbf{k} \times \mathbf{v}_h + \mathbf{F} = -f_0\mathbf{k} \times \mathbf{v}_a + \mathbf{F}, \tag{B1}$$

where $\mathbf{v}_g = \alpha f_0^{-1}\mathbf{k} \times \nabla_h p$ is the geostrophic wind and $\mathbf{v}_a = \mathbf{v}_h - \mathbf{v}_g$ is the ageostrophic wind.

In the M20 simulations, the base-state horizontal velocity is specified as $\bar{\mathbf{v}}_h = \mathbf{v}_g$, which implies that the horizontal velocity perturbation is $\mathbf{v}'_h = \mathbf{v}_h - \bar{\mathbf{v}}_h = \mathbf{v}_a$. Thus, CM1 instead solves

$$\frac{d\mathbf{v}_h}{dt} = -\alpha\nabla_h p - f_0\mathbf{k} \times \mathbf{v}'_h + \mathbf{F} = -\alpha\nabla_h p - f_0\mathbf{k} \times \mathbf{v}_a + \mathbf{F}, \tag{B2}$$

rather than (B1), or, following Davies-Jones (2021),

$$\frac{d\mathbf{v}_h}{dt} = -\alpha\nabla_h p - f_0\mathbf{k} \times \mathbf{v}_h + \mathbf{F} + \mathbf{K}, \tag{B3}$$

where $\mathbf{K} = f_0\mathbf{k} \times \bar{\mathbf{v}}_h$ is the "invented" force. M20 and others (e.g., Wilhelmson and Chen 1982; Adlerman and Droegemeier 2002) have used this approach when including surface drag so that in the horizontally homogeneous environment, where $\nabla_h p = 0$, the $-f_0\mathbf{k} \times \mathbf{v}_h$ term can balance $\mathbf{F}$ in order to yield a steady state. If $\nabla_h p = 0$ in the real atmosphere governed by (B1), then $-f_0\mathbf{k} \times \mathbf{v}_h$ cannot balance $\mathbf{F}$ by itself to yield a steady state because $-f_0\mathbf{k} \times \mathbf{v}_h$ is 90° to the right of $\mathbf{v}_h$, and therefore also approximately orthogonal to $\mathbf{F}$, given that $\mathbf{F}$ is ~180° opposite $\mathbf{v}_h$ in the boundary layer.

The balance permitted by the rhs of (B2) or (B3) leads to a quasi-steady-state hodograph that has significantly more shear than the base-state geostrophic wind profile, in addition to substantial curvature in the lowest kilometer (Fig. 1b).[10] In other words, the role of $\mathbf{K}$ is to maintain $d\mathbf{v}_h/dt \approx 0$ in the environment; thus, it acts to maintain the surface wind against the momentum loss owing to surface drag. This also implies that $\mathbf{K}$ maintains the boundary layer turbulence in the M20 simulations, because any wind blowing over a rough surface generates shear and turbulence.

The invented force is a function of z only, and therefore does not generate ζ. However, the invented force can influence the circulation about a material circuit that has a

[10] Note that the initial, base-state hodograph in Fig. 1b, which, owing to the inclusion of the invented force, is implicitly also the geostrophic hodograph, is straight. This stands in contrast to some prior studies in which hodographs exhibiting large low-level curvature have been assumed to represent the geostrophic wind profiles. Most geostrophic hodographs are fairly straight, however, as evidenced by the results of Banacos and Bluestein (2004), as well as the fact that Sutcliffe's development theorem (which implicitly assumes a straight geostrophic hodograph; Sutcliffe 1947) yields diagnoses of vertical motion that do not tend to differ radically from those obtained from the quasigeostrophic omega equation.

vertical projection, because **K** varies with height. Fortunately, it was found that the contribution of $\oint \mathbf{K} \cdot d\mathbf{x}$ to dC/dt is negligible in the M20 simulations (section 2e).

REFERENCES

Adlerman, E. J., and K. K. Droegemeier, 2002: The sensitivity of numerically simulated cyclic mesocyclogenesis to variations in model physical and computational parameters. *Mon. Wea. Rev.*, **130**, 2671–2691, https://doi.org/10.1175/1520-0493(2002)130<2671:TSONSC>2.0.CO;2.

——, ——, and R. Davies-Jones, 1999: A numerical simulation of cyclic mesocyclogenesis. *J. Atmos. Sci.*, **56**, 2045–2069, https://doi.org/10.1175/1520-0469(1999)056<2045:ANSOCM>2.0.CO;2.

Adrian, R. J., 2007: Hairpin vortex organization in wall turbulence. *Phys. Fluids*, **19**, 041301, https://doi.org/10.1063/1.2717527.

Alfonsi, G., 2006: Coherent structures of turbulence: Methods of eduction and results. *Appl. Mech. Rev.*, **59**, 307–323, https://doi.org/10.1115/1.2345370.

Anderson-Frey, A. K., Y. P. Richardson, A. R. Dean, R. L. Thompson, and B. T. Smith, 2017: Self-organizing maps for the investigation of tornadic near-storm environments. *Wea. Forecasting*, **32**, 1467–1475, https://doi.org/10.1175/WAF-D-17-0034.1.

Atkins, N. T., E. M. Glidden, and T. M. Nicholson, 2014: Observations of wall cloud formation in supercell thunderstorms during VORTEX2. *Mon. Wea. Rev.*, **142**, 4823–4838, https://doi.org/10.1175/MWR-D-14-00125.1.

Banacos, P. C., and H. B. Bluestein, 2004: Hodograph variability within analytically modeled, synoptic-scale, baroclinic systems. *Mon. Wea. Rev.*, **132**, 1448–1461, https://doi.org/10.1175/1520-0493(2004)132<1448:HVWAMS>2.0.CO;2.

Bartos, E. A., P. M. Markowski, and Y. P. Richardson, 2022: Three-dimensional thermodynamic observations in supercell thunderstorms from swarms of balloon-borne sondes. *Mon. Wea. Rev.*, **150**, 1689–1723, https://doi.org/10.1175/MWR-D-21-0122.1.

Beck, J., and C. Weiss, 2013: An assessment of low-level baroclinity and vorticity within a simulated supercell. *Mon. Wea. Rev.*, **141**, 649–669, https://doi.org/10.1175/MWR-D-11-00115.1.

Bernard, P. S., 2011: The hairpin vortex illusion. *J. Phys. Conf. Ser.*, **318**, 062004, https://doi.org/10.1088/1742-6596/318/6/062004.

——, 2015: Boundary layer vorticity and the rise of "hairpins." *Progress in Wall Turbulence 2: Understanding and Modelling*, M. Stanislas, J. Jimenez, and I. Marusic, Eds., ERCOFTAC Series, Vol. 23, Springer International, 159–169.

——, 2019: On the inherent bias of swirling strength in defining vortical structure. *Phys. Fluids*, **31**, 035107, https://doi.org/10.1063/1.5089883.

Boyer, C. H., and J. M. L. Dahl, 2020: The mechanisms responsible for large near-surface vertical vorticity within simulated supercells and quasi-linear storms. *Mon. Wea. Rev.*, **148**, 4281–4297, https://doi.org/10.1175/MWR-D-20-0082.1.

Brandes, E. A., 1978: Mesocyclone evolution and tornadogenesis: Some observations. *Mon. Wea. Rev.*, **106**, 995–1011, https://doi.org/10.1175/1520-0493(1978)106<0995:MEATSO>2.0.CO;2.

——, 1981: Finestructure of the Del City-Edmond tornadic mesocirculation. *Mon. Wea. Rev.*, **109**, 635–647, https://doi.org/10.1175/1520-0493(1981)109<0635:FOTDCE>2.0.CO;2.

——, 1984: Vertical vorticity generation and mesocyclone sustenance in tornadic thunderstorms: The observational evidence. *Mon. Wea. Rev.*, **112**, 2253–2269, https://doi.org/10.1175/1520-0493(1984)112<2253:VVGAMS>2.0.CO;2.

Browning, K. A., 1965: The evolution of tornadic storms. *J. Atmos. Sci.*, **22**, 664–668, https://doi.org/10.1175/1520-0469(1965)022<0664:TEOTS>2.0.CO;2.

Bryan, G. H., and J. M. Fritsch, 2002: A benchmark simulation for moist nonhydrostatic numerical models. *Mon. Wea. Rev.*, **130**, 2917–2928, https://doi.org/10.1175/1520-0493(2002)130<2917:ABSFMN>2.0.CO;2.

Coffer, B. E., M. D. Parker, J. M. Peters, and A. R. Wade, 2023: Supercell low-level mesocyclones: Origins of inflow and vorticity. *Mon. Wea. Rev.*, **151**, 2205–2232, https://doi.org/10.1175/MWR-D-22-0269.1.

Dahl, J. M. L., 2015: Near-ground rotation in simulated supercells: On the robustness of the baroclinic mechanism. *Mon. Wea. Rev.*, **143**, 4929–4942, https://doi.org/10.1175/MWR-D-15-0115.1.

——, M. D. Parker, and L. J. Wicker, 2014: Imported and storm-generated near-ground vertical vorticity in a simulated supercell. *J. Atmos. Sci.*, **71**, 3027–3051, https://doi.org/10.1175/JAS-D-13-0123.1.

Davidson, P., 2015: *Turbulence: An Introduction for Scientists and Engineers*. 2nd ed. Oxford University Press, 630 pp.

Davies-Jones, R. P., 1982a: A new look at the vorticity equation with application to tornadogenesis. Preprints, *12th Conf. on Severe Local Storms*, San Antonio, TX, Amer. Meteor. Soc., 249–252.

——, 1982b: Observational and theoretical aspects of tornadogenesis. *Intense Atmospheric Vortices*, L. Bengtsson and J. Lighthill, Eds., Springer, 175–189.

——, 1984: Streamwise vorticity: The origin of updraft rotation in supercell storms. *J. Atmos. Sci.*, **41**, 2991–3006, https://doi.org/10.1175/1520-0469(1984)041<2991:SVTOOU>2.0.CO;2.

——, 2000: A Lagrangian model for baroclinic genesis of mesoscale vortices. Part I: Theory. *J. Atmos. Sci.*, **57**, 715–736, https://doi.org/10.1175/1520-0469(2000)057<0715:ALMFBG>2.0.CO;2.

——, 2015: A review of supercell and tornado dynamics. *Atmos. Res.*, **158–159**, 274–291, https://doi.org/10.1016/j.atmosres.2014.04.007.

——, 2021: Invented forces in supercell models. *J. Atmos. Sci.*, **78**, 2927–2939, https://doi.org/10.1175/JAS-D-21-0082.1.

——, and H. Brooks, 1993: Mesocyclogenesis from a theoretical perspective. *The Tornado: Its Structure, Dynamics, Prediction, and Hazards*, *Geophys. Monogr.*, Vol. 79, Amer. Geophys. Union, 105–114, https://doi.org/10.1029/GM079p0105.

——, and P. M. Markowski, 2021: Circulation around a constrained curve: An alternative analysis tool for diagnosing the origins of tornado rotation in numerical supercell simulations. *J. Atmos. Sci.*, **78**, 2895–2909, https://doi.org/10.1175/JAS-D-21-0020.1.

——, R. J. Trapp, and H. B. Bluestein, 2001: Tornadoes and tornadic storms. *Severe Convective Storms*, *Meteor. Monogr.*, No. 28, Amer. Meteor. Soc., 167–222, https://doi.org/10.1175/0065-9401-28.50.167.

Deardorff, J. W., 1980: Stratocumulus-capped mixed layer derived from a three-dimensional model. *Bound.-Layer Meteor.*, **18**, 495–527, https://doi.org/10.1007/BF00119502.

Doswell, C. A., III, and D. W. Burgess, 1993: Tornadoes and tornadic storms: A review of conceptual models. *The Tornado: Its Structure, Dynamics, Prediction, and Hazards*, *Geophys. Monogr.*, Vol. 79, Amer. Geophys. Union, 161–172, https://doi.org/10.1029/GM079p0161.

Dutton, J. A., 1986: *The Ceaseless Wind: An Introduction to the Theory of Atmospheric Motion*. Dover, 617 pp.

Eitel-Amor, G., R. Örlü, P. Schlatter, and O. Flores, 2015: Hairpin vortices in turbulent boundary layers. *Phys. Fluids*, **27**, 025108, https://doi.org/10.1063/1.4907783.

Emanuel, K. A., 1994: *Atmospheric Convection*. Oxford University Press, 580 pp.

Fischer, J., and J. M. L. Dahl, 2022: Transition of near-ground vorticity dynamics during tornadogenesis. *J. Atmos. Sci.*, **79**, 467–483, https://doi.org/10.1175/JAS-D-21-0181.1.

Forbes, G. S., 1981: On the reliability of hook echoes as tornado indicators. *Mon. Wea. Rev.*, **109**, 1457–1466, https://doi.org/10.1175/1520-0493(1981)109<1457:OTROHE>2.0.CO;2.

Frame, J., and P. Markowski, 2010: Numerical simulations of radiative cooling beneath the anvils of supercell thunderstorms. *Mon. Wea. Rev.*, **138**, 3024–3047, https://doi.org/10.1175/2010MWR3177.1.

——, and ——, 2013: Dynamical influences of anvil shading on simulated supercell thunderstorms. *Mon. Wea. Rev.*, **141**, 2802–2820, https://doi.org/10.1175/MWR-D-12-00146.1.

Fujita, T., 1958: Mesoanalysis of the Illinois tornadoes of 9 April 1953. *J. Meteor.*, **15**, 288–296, https://doi.org/10.1175/1520-0469(1958)015<0288:MOTITO>2.0.CO;2.

——, 1960: A detailed analysis of the Fargo tornadoes of June 20, 1957. U.S. Weather Bureau Research Paper 42, 67 pp., https://www.weather.gov/media/publications/assessments/Fargo%20Tornadoes%20June%2020%201957.pdf.

——, 1973: Proposed mechanism of tornado formation from rotating thunderstorms. Preprints, *Eighth Conf. on Severe Local Storms*, Denver, CO, Amer. Meteor. Soc., 191–196.

——, 1981: Tornadoes and downbursts in the context of generalized planetary scales. *J. Atmos. Sci.*, **38**, 1511–1534, https://doi.org/10.1175/1520-0469(1981)038<1511:TADITC>2.0.CO;2.

Guarriello, F., C. J. Nowotarski, and C. C. Epifanio, 2018: Effects of the low-level wind profile on outflow position and near-surface vertical vorticity in simulated supercell thunderstorms. *J. Atmos. Sci.*, **75**, 731–753, https://doi.org/10.1175/JAS-D-17-0174.1.

Jeong, J., and F. Hussain, 1995: On the identification of a vortex. *J. Fluid Mech.*, **285**, 69–94, https://doi.org/10.1017/S0022112095000462.

Khanna, S., and J. G. Brasseur, 1998: Three-dimensional buoyancy- and shear-induced local structure of the atmospheric boundary layer. *J. Atmos. Sci.*, **55**, 710–743, https://doi.org/10.1175/1520-0469(1998)055<0710:TDBASI>2.0.CO;2.

Klemp, J. B., and R. B. Wilhelmson, 1978: The simulation of three-dimensional convective storm dynamics. *J. Atmos. Sci.*, **35**, 1070–1096, https://doi.org/10.1175/1520-0469(1978)035<1070:TSOTDC>2.0.CO;2.

——, and R. Rotunno, 1983: A study of the tornadic region within a supercell thunderstorm. *J. Atmos. Sci.*, **40**, 359–377, https://doi.org/10.1175/1520-0469(1983)040<0359:ASOTTR>2.0.CO;2.

——, R. B. Wilhelmson, and P. S. Ray, 1981: Observed and numerically simulated structure of a mature supercell thunderstorm. *J. Atmos. Sci.*, **38**, 1558–1580, https://doi.org/10.1175/1520-0469(1981)038<1558:OANSSO>2.0.CO;2.

Kosiba, K., J. Wurman, Y. Richardson, P. Markowski, P. Robinson, and J. Marquis, 2013: Genesis of the Goshen County, Wyoming, tornado on 5 June 2009 during VORTEX2. *Mon. Wea. Rev.*, **141**, 1157–1181, https://doi.org/10.1175/MWR-D-12-00056.1.

Lemon, L. R., and C. A. Doswell III, 1979: Severe thunderstorm evolution and mesocyclone structure as related to tornadogenesis. *Mon. Wea. Rev.*, **107**, 1184–1197, https://doi.org/10.1175/1520-0493(1979)107<1184:STEAMS>2.0.CO;2.

Lewellen, W. S., 1993: Tornado vortex theory. *The Tornado: Its Structure, Dynamics, Prediction, and Hazards*, *Geophys. Monogr.*, Vol. 79, Amer. Geophys. Union, 19–39, https://doi.org/10.1029/GM079p0019.

Ludlam, F. H., 1963: Severe local storms: A review. *Severe Local Storms*, *Meteor. Monogr.*, No. 27, Amer. Meteor. Soc., 1–30, https://doi.org/10.1007/978-1-940033-56-3_1.

Mansell, E. R., and C. L. Ziegler, 2013: Aerosol effects on simulated storm electrification and precipitation in a two-moment bulk microphysics model. *J. Atmos. Sci.*, **70**, 2032–2050, https://doi.org/10.1175/JAS-D-12-0264.1.

——, ——, and E. C. Bruning, 2010: Simulated electrification of a small thunderstorm with two-moment bulk microphysics. *J. Atmos. Sci.*, **67**, 171–194, https://doi.org/10.1175/2009JAS2965.1.

Markowski, P. M., 2002: Hook echoes and rear-flank downdrafts: A review. *Mon. Wea. Rev.*, **130**, 852–876, https://doi.org/10.1175/1520-0493(2002)130<0852:HEARFD>2.0.CO;2.

——, 2016: An idealized numerical simulation investigation of the effects of surface drag on the development of near-surface vertical vorticity in supercell thunderstorms. *J. Atmos. Sci.*, **73**, 4349–4385, https://doi.org/10.1175/JAS-D-16-0150.1.

——, 2020: What is the intrinsic predictability of tornadic supercell thunderstorms? *Mon. Wea. Rev.*, **148**, 3157–3180, https://doi.org/10.1175/MWR-D-20-0076.1.

——, and Y. P. Richardson, 2009: Tornadogenesis: Our current understanding, forecasting considerations, and questions to guide future research. *Atmos. Res.*, **93**, 3–10, https://doi.org/10.1016/j.atmosres.2008.09.015.

——, and ——, 2014a: What we know and don't know about tornado formation. *Phys. Today*, **67**, 26–31, https://doi.org/10.1063/PT.3.2514.

——, and ——, 2014b: The influence of environmental low-level shear and cold pools on tornadogenesis: Insights from idealized simulations. *J. Atmos. Sci.*, **71**, 243–275, https://doi.org/10.1175/JAS-D-13-0159.1.

——, and G. H. Bryan, 2016: LES of laminar flow in the PBL: A potential problem for convective storm simulations. *Mon. Wea. Rev.*, **144**, 1841–1850, https://doi.org/10.1175/MWR-D-15-0439.1.

——, E. N. Rasmussen, J. M. Straka, and D. C. Dowell, 1998: Observations of low-level baroclinity generated by anvil shadows. *Mon. Wea. Rev.*, **126**, 2942–2958, https://doi.org/10.1175/1520-0493(1998)126<2942:OOLLBG>2.0.CO;2.

——, C. Hannon, J. Frame, E. Lancaster, A. Pietrycha, R. Edwards, and R. Thompson, 2003: Characteristics of vertical wind profiles near supercells obtained from the Rapid Update Cycle. *Wea. Forecasting*, **18**, 1262–1272, https://doi.org/10.1175/1520-0434(2003)018<1262:COVWPN>2.0.CO;2.

——, Y. Richardson, E. Rasmussen, J. Straka, R. Davies-Jones, and R. J. Trapp, 2008: Vortex lines within low-level mesocyclones obtained from pseudo-dual-Doppler radar observations. *Mon. Wea. Rev.*, **136**, 3513–3535, https://doi.org/10.1175/2008MWR2315.1.

——, M. Majcen, Y. Richardson, J. Marquis, and J. Wurman, 2011: Characteristics of the wind field in three nontornadic low-level mesocyclones observed by the Doppler on Wheels radars. *Electron. J. Severe Storms Meteor.*, **6** (3), https://doi.org/10.55599/ejssm.v6i3.30.

——, and Coauthors, 2012a: The pretornadic phase of the Goshen County, Wyoming, supercell of 5 June 2009 intercepted by VORTEX2. Part I: Evolution of kinematic and surface thermodynamic fields. *Mon. Wea. Rev.*, **140**, 2887–2915, https://doi.org/10.1175/MWR-D-11-00336.1.

——, and Coauthors, 2012b: The pretornadic phase of the Goshen County, Wyoming, supercell of 5 June 2009 intercepted by VORTEX2. Part II: Intensification of low-level rotation. *Mon. Wea. Rev.*, **140**, 2916–2938, https://doi.org/10.1175/MWR-D-11-00337.1.

——, Y. Richardson, and G. Bryan, 2014: The origins of vortex sheets in a simulated supercell thunderstorm. *Mon. Wea. Rev.*, **142**, 3944–3954, https://doi.org/10.1175/MWR-D-14-00162.1.

——, N. T. Lis, D. D. Turner, T. R. Lee, and M. S. Buban, 2019: Observations of near-surface vertical wind profiles and vertical momentum fluxes from VORTEX-SE 2017: Comparisons to Monin–Obukhov similarity theory. *Mon. Wea. Rev.*, **147**, 3811–3824, https://doi.org/10.1175/MWR-D-19-0091.1.

Marquis, J., Y. Richardson, P. Markowski, D. Dowell, and J. Wurman, 2012: Tornado maintenance investigated with high-resolution dual-Doppler and EnKF analysis. *Mon. Wea. Rev.*, **140**, 3–27, https://doi.org/10.1175/MWR-D-11-00025.1.

Mashiko, W., 2016: A numerical study of the 6 May 2012 Tsukuba City supercell tornado. Part II: Mechanisms of tornadogenesis. *Mon. Wea. Rev.*, **144**, 3077–3098, https://doi.org/10.1175/MWR-D-15-0122.1.

Moin, P., and J. Kim, 1985: The structure of the vorticity field in turbulent channel flow. Part 1: Analysis of instantaneous fields and statistical correlations. *J. Fluid Mech.*, **155**, 441–464, https://doi.org/10.1017/S0022112085001896.

Nowotarski, C. J., and P. M. Markowski, 2016: Modifications to the near-storm environment induced by simulated supercell thunderstorms. *Mon. Wea. Rev.*, **144**, 273–293, https://doi.org/10.1175/MWR-D-15-0247.1.

——, ——, Y. P. Richardson, and G. H. Bryan, 2015: Supercell low-level mesocyclones in simulations with a sheared convective boundary layer. *Mon. Wea. Rev.*, **143**, 272–297, https://doi.org/10.1175/MWR-D-14-00151.1.

Okubo, A., 1970: Horizontal dispersion of floatable particles in the vicinity of velocity singularities such as convergences. *Deep-Sea Res. Oceanogr. Abstr.*, **17**, 445–454, https://doi.org/10.1016/0011-7471(70)90059-8.

Orf, L., R. Wilhelmson, B. Lee, C. Finley, and A. Houston, 2017: Evolution of a long-track violent tornado within a simulated supercell. *Bull. Amer. Meteor. Soc.*, **98**, 45–68, https://doi.org/10.1175/BAMS-D-15-00073.1.

Orlanski, I., 1975: A rational subdivision of scales for atmospheric processes. *Bull. Amer. Meteor. Soc.*, **56**, 527–530, https://doi.org/10.1175/1520-0477-56.5.527.

Parker, M. D., 2023: How well must surface vorticity be organized for tornadogenesis? *J. Atmos. Sci.*, **80**, 1433–1448, https://doi.org/10.1175/JAS-D-22-0195.1.

——, and J. M. L. Dahl, 2015: Production of near-surface vertical vorticity by idealized downdrafts. *Mon. Wea. Rev.*, **143**, 2795–2816, https://doi.org/10.1175/MWR-D-14-00310.1.

Riganti, C. J., and A. L. Houston, 2017: Rear-flank outflow dynamics and thermodynamics in the 10 June 2010 Last Chance, Colorado, supercell. *Mon. Wea. Rev.*, **145**, 2487–2504, https://doi.org/10.1175/MWR-D-16-0128.1.

Roberts, B., and M. Xue, 2017: The role of surface drag in mesocyclone intensification leading to tornadogenesis within an idealized supercell simulation. *J. Atmos. Sci.*, **74**, 3055–3077, https://doi.org/10.1175/JAS-D-16-0364.1.

——, ——, A. D. Schenkman, and D. T. Dawson II, 2016: The role of surface drag in tornadogenesis within an idealized supercell simulation. *J. Atmos. Sci.*, **73**, 3371–3395, https://doi.org/10.1175/JAS-D-15-0332.1.

——, ——, and D. T. Dawson II, 2020: The effect of surface drag strength on mesocyclone intensification and tornadogenesis in idealized supercell simulations. *J. Atmos. Sci.*, **77**, 1699–1721, https://doi.org/10.1175/JAS-D-19-0109.1.

Robinson, S. K., 1991: Coherent motions in the turbulent boundary layer. *Annu. Rev. Fluid Mech.*, **23**, 601–639, https://doi.org/10.1146/annurev.fl.23.010191.003125.

Rotunno, R., 1993: Supercell thunderstorm modeling and theory. *The Tornado: Its Structure, Dynamics, Prediction, and Hazards*, *Geophys. Monogr.*, Vol. 79, Amer. Geophys. Union, 57–73, https://doi.org/10.1029/GM079p0057.

——, and J. B. Klemp, 1982: The influence of the shear-induced pressure gradient on thunderstorm motion. *Mon. Wea. Rev.*, **110**, 136–151, https://doi.org/10.1175/1520-0493(1982)110<0136:TIOTSI>2.0.CO;2.

——, and ——, 1985: On the rotation and propagation of simulated supercell thunderstorms. *J. Atmos. Sci.*, **42**, 271–292, https://doi.org/10.1175/1520-0469(1985)042<0271:OTRAPO>2.0.CO;2.

——, ——, and M. L. Weisman, 1988: A theory for strong, long-lived squall lines. *J. Atmos. Sci.*, **45**, 463–485, https://doi.org/10.1175/1520-0469(1988)045<0463:ATFSLL>2.0.CO;2.

——, P. M. Markowski, and G. H. Bryan, 2017: "Near-ground" vertical vorticity in supercell thunderstorm models. *J. Atmos. Sci.*, **74**, 1757–1766, https://doi.org/10.1175/JAS-D-16-0288.1.

Schenkman, A. D., M. Xue, and M. Hu, 2014: Tornadogenesis in a high-resolution simulation of the 8 May 2003 Oklahoma City supercell. *J. Atmos. Sci.*, **71**, 130–154, https://doi.org/10.1175/JAS-D-13-073.1.

Schlesinger, R. E., 1975: A three-dimensional numerical model of an isolated deep convective cloud: Preliminary results. *J. Atmos. Sci.*, **32**, 934–957, https://doi.org/10.1175/1520-0469(1975)032<0934:ATDNMO>2.0.CO;2.

Stout, G. E., and F. A. Huff, 1953: Radar records Illinois tornadogenesis. *Bull. Amer. Meteor. Soc.*, **34**, 281–284, https://doi.org/10.1175/1520-0477-34.6.281.

Straka, J., E. Rasmussen, R. P. Davies-Jones, and P. Markowski, 2007: An observational and idealized numerical examination of low-level counter-rotating vortices toward the rear flank of supercells. *Electron. J. Severe Storms Meteor.*, **2** (8), https://doi.org/10.55599/ejssm.v2i8.13.

Sutcliffe, R. C., 1947: A contribution to the problem of development. *Quart. J. Roy. Meteor. Soc.*, **73**, 370–383, https://doi.org/10.1002/qj.49707331710.

Tao, T., and T. Tamura, 2020: Numerical study of the 6 May 2012 Tsukuba supercell tornado: Vorticity sources responsible for tornadogenesis. *Mon. Wea. Rev.*, **148**, 1205–1228, https://doi.org/10.1175/MWR-D-19-0095.1.

Theodorsen, T., 1952: Mechanism of turbulence. *Proc. Second Midwestern Conf. on Fluid Mech.*, Columbus, OH, Ohio State University, 1–19.

——, 1955: The structure of turbulence. *50 Jahre Grenzschictforschung*, H. Gortler and W. Tollmein, Eds., Vieweg and Teubner Verlag, 55–62.

Thompson, R. L., R. Edwards, J. A. Hart, K. L. Elmore, and P. Markowski, 2003: Close proximity soundings within supercell environments obtained from the Rapid Update Cycle. *Wea. Forecasting*, **18**, 1243–1261, https://doi.org/10.1175/1520-0434(2003)018<1243:CPSWSE>2.0.CO;2.

Wakimoto, R. M., C. Liu, and H. Cai, 1998: The Garden City, Kansas, storm during VORTEX 95. Part I: Overview of the storm's life cycle and mesocyclogenesis. *Mon. Wea. Rev.*, **126**,

372–392, https://doi.org/10.1175/1520-0493(1998)126<0372:TGCKSD>2.0.CO;2.

Wang, A., Y. Pan, and P. M. Markowski, 2020: The influence of turbulence memory on idealized tornado simulations. *Mon. Wea. Rev.*, **148**, 4875–4892, https://doi.org/10.1175/MWR-D-20-0031.1.

——, ——, G. H. Bryan, and P. M. Markowski, 2023: Modeling near-surface turbulence in large-eddy simulations of a tornado: An application of thin boundary-layer equations. *Mon. Wea. Rev.*, **151**, 1587–1607, https://doi.org/10.1175/MWR-D-22-0060.1.

Weiss, J., 1991: The dynamics of enstrophy transfer in two-dimensional hydrodynamics. *Physica D*, **48**, 273–294, https://doi.org/10.1016/0167-2789(91)90088-Q.

Wicker, L. J., and R. B. Wilhelmson, 1995: Simulation and analysis of tornado development and decay within a three-dimensional supercell thunderstorm. *J. Atmos. Sci.*, **52**, 2675–2703, https://doi.org/10.1175/1520-0469(1995)052<2675:SAAOTD>2.0.CO;2.

Wilhelmson, R. B., and C.-S. Chen, 1982: A simulation of the development of successive cells along a cold outflow boundary. *J. Atmos. Sci.*, **39**, 1466–1483, https://doi.org/10.1175/1520-0469(1982)039<1466:ASOTDO>2.0.CO;2.

——, and L. J. Wicker, 2001: Numerical modeling of severe local storms. *Severe Convective Storms*, *Meteor. Monogr.*, No. 50, Amer Meteor. Soc., 123–166, https://doi.org/10.1007/978-1-935704-06-5_4.

Wurman, J., D. Dowell, Y. Richardson, P. Markowski, E. Rasmussen, D. Burgess, L. Wicker, and H. B. Bluestein, 2012: The second Verification of the Origins of Rotation in Tornadoes Experiment 2: VORTEX2. *Bull. Amer. Meteor. Soc.*, **93**, 1147–1170, https://doi.org/10.1175/BAMS-D-11-00010.1.

Yokota, S., H. Niino, H. Seko, M. Kunii, and H. Yamauchi, 2018: Important factors for tornadogenesis as revealed by high-resolution ensemble forecasts of the Tsukuba supercell tornado of 6 May 2012 in Japan. *Mon. Wea. Rev.*, **146**, 1109–1132, https://doi.org/10.1175/MWR-D-17-0254.1.

Young, G. S., D. A. R. Kristovich, M. R. Hjelmfelt, and R. C. Foster, 2002: Rolls, streets, waves, and more: A review of quasi-two-dimensional structures in the atmospheric boundary layer. *Bull. Amer. Meteor. Soc.*, **83**, 997–1002,https://doi.org/10.1175/1520-0477(2002)083<0997:RSWAMA>2.3.CO;2.

Ziegler, C. L., 1985: Retrieval of thermal and microphysical variables in observed convective storms. Part I: Model development and preliminary testing. *J. Atmos. Sci.*, **42**, 1487–1509, https://doi.org/10.1175/1520-0469(1985)042<1487:ROTAMV>2.0.CO;2.

——, E. N. Rasmussen, T. R. Shepherd, A. I. Watson, and J. M. Straka, 2001: The evolution of low-level rotation in the 29 May 1994 Newcastle–Graham, Texas, storm complex during VORTEX. *Mon. Wea. Rev.*, **129**, 1339–1368, https://doi.org/10.1175/1520-0493(2001)129<1339:TEOLLR>2.0.CO;2.